Chapter 18
Thermal Remote Sensing of Active Vegetation Fires and Biomass Burning Events

Martin J. Wooster, Gareth Roberts, Alistair M.S. Smith, Joshua Johnston, Patrick Freeborn, Stefania Amici, and Andrew T. Hudak

Abstract Thermal remote sensing is widely used in the detection, study, and management of biomass burning occurring in open vegetation fires. Such fires may be planned for land management purposes, may occur as a result of a malicious or accidental ignition by humans, or may result from lightning or other natural phenomena. Under suitable conditions, fires may spread rapidly and extensively, affecting the land cover properties of large areas, and releasing a wide variety of gases and particulates directly into Earth's troposphere. On average, around 3.4 % of the Earth's terrestrially vegetated area burns annually in this way. Vegetation fires inevitably involve high temperatures, so thermal remote sensing is well suited to its identification and study. Here we review the theoretical basis of the key approaches used to (1) detect actively burning fires; (2) characterize sub-pixel fires; and (3) estimate fuel consumption and smoke emissions. We describe the types of

M.J. Wooster (✉) • P. Freeborn
Department of Geography, King's College London (KCL), Strand, London, UK
e-mail: Martin.wooster@kcl.ac.uk

G. Roberts
Geography and Environment, University of Southampton, Southampton, UK

A.M.S. Smith
Department of Forest Resources, College of Natural Resources, University of Idaho, Moscow, ID, USA

J. Johnston
Department of Geography, King's College London (KCL), Strand, London, UK

Canadian Forest Service, Natural Resources Canada, Great Lakes Forestry Centre, Sault Ste. Marie, ON, Canada

S. Amici
Istituto Nazionale di Geofisica e Vulcanologia (INGV), Rome, Italy

A.T. Hudak
US Forest Service Rocky Mountain Research Station, Moscow Forestry Sciences Laboratory, Moscow, ID, USA

C. Kuenzer and S. Dech (eds.), *Thermal Infrared Remote Sensing: Sensors, Methods, Applications*, Remote Sensing and Digital Image Processing 17,
DOI 10.1007/978-94-007-6639-6_18,

airborne and spaceborne systems that deliver data for use with these active fire thermal remote sensing methods, and provide some examples of how operational fire management and fire research have both benefited from the resulting information. We commence with a brief review of the significance and magnitude of biomass burning, both within the 'whole Earth' system and in more regional situations, aiming to highlight why thermal remote sensing has become so important to the study and management of open vegetation burning.

18.1 Significance of Global Biomass Burning

Biomass burning is a key process shaping the Earth system, affecting the terrestrial biosphere and atmosphere through the combustion of vegetation and organic soils, and transferring the vast bulk of their chemical constituents directly into the troposphere. Seiler and Crutzen (1980) are often credited with providing amongst the earliest scientific insights into the large scale significance of biomass burning. However, in fact in the late nineteenth century von Danckelman (1884) already drew attention to its magnitude and potential consequence (Brönnimann et al. 2009).

Detailed information on the many ways in which biomass burning impacts Earth's land and atmospheric properties are included in reviews such as Jacobson et al. (2000), Lavorel et al. (2007), Bowman et al.(2009), and Akagi et al. (2011). In the context of this chapter, it is sufficient that the reader appreciates the huge areas and very significant mass of vegetation and organic soil globally affected, in order to comprehend the need for large-scale fire assessment and monitoring via thermal remote sensing methods.

Amongst the most recent burned area estimates are those of Giglio et al. (2010), who used datasets derived from (mainly optical) satellite remote sensing to estimate that between 1997 and 2008 global vegetation fires cumulatively burned 44.5 million km^2, equivalent to the combined area of North and South America, or ~40 % of Earth's total terrestrially vegetated area. Some of this burning is planned and under human control; other areas are ignited and left to spread largely unhindered by man; still others are ignited accidentally or by natural phenomena (primarily lightning). Much of the 44.5 million km^2 burned includes re-burning in the savannah ecosystems of Africa, South America, and Australia. Here, a combination of large areas of highly combustible grassy fuels, annually reoccurring 'fire seasons', a ready supply of human ignition sources, and rapid post-fire vegetation recovery, combine to support mean fire return intervals that can be as short as 1–3 years. Indeed, such burning is in part responsible for maintaining the structure and function of savannah ecosystems, which in total constitute ~20 % of Earth's land surface area (Bond and van Wilgen 1996).

The maps of Giglio et al. (2010) indicate that, on average, ~3.4 % of the Earth's terrestrially vegetated area burns annually, with resulting large scale effects on surface properties and land cover, landscape heterogeneity, and ecology (e.g. Turner et al. 1994; De Bano et al. 1998; Wallace 2004; Bond and Keeley 2005;

Pausas and Keeley 2009). Clearly, the importance of a wide-scale disturbance phenomena like biomass burning is highly significant within the Earth system, This includes impacts from large-scale slash-and-burn practices and severe forest fires, particularly in disturbed areas, that contribute significantly to tropical deforestation and forest degradation (Bond et al. 2005; Cochrane 2003; Wooster et al. 2012).

In addition to altering land surface dynamics, vegetation fires greatly affect Earth's atmospheric composition. They release an amount of carbon to the atmosphere equivalent to perhaps around one quarter, possibly more, of global annual industrial emissions (van der Werf et al. 2010); mostly in the form of CO_2. Furthermore, van der Werf et al. (2009) demonstrate that deforestation and tropical peatland fire emissions (which unlike savannah emissions are not rapidly re-sequestered) equate to the equivalent of perhaps 15 ± 5 % of industrial CO_2 emissions. In addition to CO_2, biomass burning releases a vast range of other trace gas and particulate species involved in important atmospheric processes (e.g. Andreae and Merlet 2001; Crutzen and Andreae 1990; Kaufman et al. 2002). Studies such as Page et al. (2002), van der Werf et al. (2004) and Wooster et al. (2012) indicate that land clearance activities, coupled with periods of extreme 'fire weather' such as El Niño related drought, can result in massive increases in the number and size of regional vegetation fires, which sometimes have globally detectable effects on atmospheric composition through the release of these compounds (e.g. Simmonds et al. 2005). At the local to regional scale, the potential loss of property and lives during large fire events, and the impacts on national fire management budgets, can be considerable (Lynch 2004), and fires may result in major smoke and haze events that can greatly impact air quality and human health (Kunii et al. 2002; Naeher et al. 2007).

Since vegetation fires occur over wide areas, are sporadic and rapidly changing in nature, are international in scope, and often occur in isolated regions, remote sensing has become a key tool in their identification and study. Thermal remote sensing is used widely to map fire extents, examine fire regimes, characterize fire impacts, and estimate and characterize the chemical composition of fire emissions (e.g. McMillan et al. 2003; Coheur et al. 2009; Wooster et al. 2011). The focus of this chapter is primarily to explore the background and techniques related to the thermal remote sensing of the actively burning fires themselves. Hence, we review the theory to both fire detection and fire characterization from airborne and spaceborne platforms, and their use in support of both research and operational applications.

18.2 Thermal Remote Sensing of Vegetation Combustion

Vegetation combustion is a complex process that involves simultaneous coupled heat and mass transfer, with the chemical reactions and fluid flows made more complex by the nature and non-uniformity of 'natural' fuels (Jenkins et al. 1998). Vegetation combustion involves significant energy releases, including as radiant energy, and hence is able to be targeted using thermal remote sensing methods.

Biomass consists mainly of cellulose, hemi-cellulose, and lignin produced through the process of photosynthesis, along with water, small amounts of nitrogen, sulphur, and some inorganic compounds that remain as ash after a fire (Jenkins et al. 1998). The polymeric organic compounds that comprise plant material can be generally described by the chemical formula $C_6H_9O_4$ (Byram 1959), and the nature of the chemical reaction involved in the complete air-based combustion of vegetation fuel of moisture content M% by dry weight can be represented by:

$$\begin{aligned} &4\,C_6H_9O_4 + 25O_2 + [0.322\,M\,H_2O + 94.0N_2] \\ &\rightarrow 24\,CO_2 + 18\,H_2O + [0.322\,M\,H_2O + 94.0\,N_2] + 11.6 \times 10^9\,J \end{aligned} \tag{18.1}$$

See Byram (1959) and Ward (2001) for a complete description of Eq. (18.1), where the moisture in the fuel and nitrogen in the air are shown as bracketed quantities since they do not take part in the combustion reaction. The same equation also describes decomposition, a much slower form of oxidation; both combustion and decomposition are essentially the reverse of photosynthesis. By dry weight, vegetation fuels are approximately 50 % carbon, 44 % oxygen and 5 % hydrogen (Ward 2001), and when burned completely approximately half the dry mass is converted to CO_2 and half to water in the manner described in Eq. (18.1). The 'heat of combustion' released by this energetic reaction equates to ~20.1 MJ per kilogram of dry fuel burned, and varies by less than 10 % between the woody and herbaceous fuel types occurring in most forests and savannahs (Stocks et al. 1997; Trollope 2002). Some of the released energy is used as the latent heat of vaporisation for the water contained in the fuel and formed by the reaction, so the actual 'heat yield' (or 'low heat of combustion') from vegetation fires burning under natural conditions is somewhat lowered (Byram 1959; Pyne 1984). Mean values are often ~18 MJ kg^{-1} of dry fuel burned (e.g. Cheney and Sullivan 2008), and depend on factors such as the exact fuel moisture content and combustion completeness (Byram 1959; Alexander 1982; Dietenberger 2002). Incomplete combustion results in the production of significant amounts of additional compounds beyond carbon dioxide and water vapor, including carbon monoxide, hydrocarbons, and black carbon particles (each of which are some of the major constituents of 'smoke'). The proportion of a fire's heat yield released as radiation varies with fire characteristics and is still a subject of active research (e.g. Freeborn et al. 2008). Byram (1959) estimated around 10–20 % of a fire's energy is radiated away from the combustion zone in the form of electromagnetic radiation of different wavelengths, which is then available to be measured by remote sensing devices. Figure 18.1 shows some example data of a forest fire targeted by an airborne imaging spectrometer acquisition that collected multispectral visible (VIS), near infrared (NIR) and shortwave infrared (SWIR) imagery and spectra.

In Fig. 18.1, the majority of the visible (VIS) wavelength radiation measured at point A in the inset is actually emitted radiation from the burning fuel, and its strong increase with increasing wavelength can be seen in Fig. 18.1c when compared to point B. At point B, the measurement of the fires emitted VIS wavelength radiation is strongly hindered by the overlying smoke. Our eyes 'see' only this VIS wavelength radiation emitted by such burning vegetation; but more of the energy is

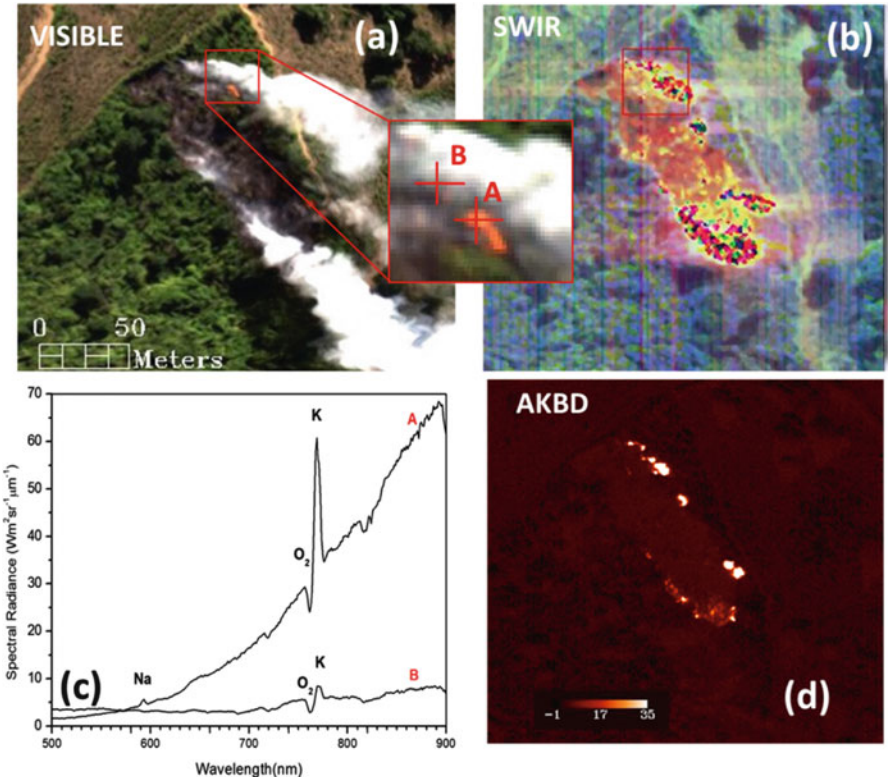

Fig. 18.1 Forest fire remote sensing data from the HYPER–SIM.GA airborne spectrometer imagery described in Amici et al. (2011). (**a**) True colour composite along with a magnification better highlighting an area of emitted visible wavelength radiation resulting from flaming combustion. (**b**) False color composite of the same area derived using shortwave infrared wavebands, illustrating the ability to penetrate the smoke at these wavelengths and highlight both actively burning and already burned areas. (**c**) Spectra of location A (flaming fire; relatively smoke-free) and B (smoke-covered fire) identified in the magnified inset of (a). (**d**) The 'Advanced Potassium Band Difference (*AKBD*)' metric of Amici et al. (2011) which uses NIR spectral measurements inside and outside of the potassium absorption line region noted in (c) to identify flaming areas. The image is shown at the same scale and covering the same areas as (a). The location of flaming areas, even those burning underneath smoke, are clearly discernible using this simple multispectral technique

actually emitted at longer infrared (IR) wavelengths. The majority of this emitted energy is 'blackbody' type radiation emitted in accordance with Planck's radiation law, and flames have very high emissivity's at flame depths greater than a few meters and so are strong IR sources (e.g. Àgueda et al. 2010; Pastor et al. 2002). The spectra of point A included in Fig. 18.1c demonstrates the characteristic shape of a Planck curve, though the curve is clearly peaking at an IR wavelength somewhat beyond the maximum wavelength shown in the plot. As Fig. 18.1b shows, the smoke also becomes increasingly transparent at such longer (IR) wavelengths, and the sensors SWIR wavebands easily identify both areas of emitted SWIR radiation from the burning fuel and the change in reflected solar SWIR radiation resulting from areas of already burned vegetation, even through the smoke.

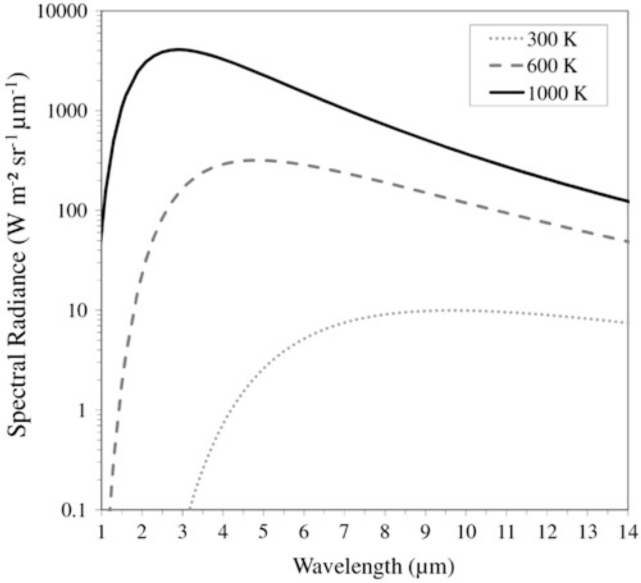

Fig. 18.2 Modeled thermal emission from a 1000, 600, and 300 K object, representing a flame, a smoldering fire, and the ambient background respectively. Calculations were made using Planck's Law assuming blackbody behavior. The shift of the peak wavelength of thermal emission as the emitted temperature increases is described by Wien's Displacement Law. Note the logarithmic scale of the y-axis, and so the large increase in thermally emitted spectral radiance at all wavelengths as temperature increases from ambient to flaming conditions. Also not that increases in the middle infrared (MIR) spectral region (3–5 μm atmospheric window) are of a much greater magnitude than those in the long-wave infrared (LWIR) spectral region (8–14 μm atmospheric window)

Superimposed on the Planckian thermal emission shown in Fig. 18.1c is near infrared (NIR) line emission from thermally excited trace elements within the burning vegetation, in this case potassium (K) ~0.76–0.77 μm, and sodium (Na) at 0.59 μm (Amici et al. 2011). This signature can also be used to identify specific areas of flaming activity through smoke (Fig. 18.1d), since the production of this line emission requires the high temperatures specific to flaming rather than smoldering combustion. Additional band radiation is also superimposed on the Planckian thermal signatures, due to the H_2O, CO_2 and other hot gases produced during combustion. This occurs within particular absorption and emission spectral regions, sometimes at wavelengths outside of the main 'atmospheric window' regions normally used to image the Earth. See Boulet et al. (2011) for a detailed discussion of such gaseous thermal emission and absorption features. Some active fire remote sensing applications make use of these types of line emission and gaseous band emission features, but most rely on the detection of Planckian thermal emission signatures, most commonly in the middle IR atmospheric window (MIR; 3–5 μm) where fire IR emissions generally peak and where solar radiation signal is lower than in the SWIR (Fig. 18.2). Observations in the longwave IR atmospheric window (LWIR; 8–14 μm) are also commonly used to enhance fire detection

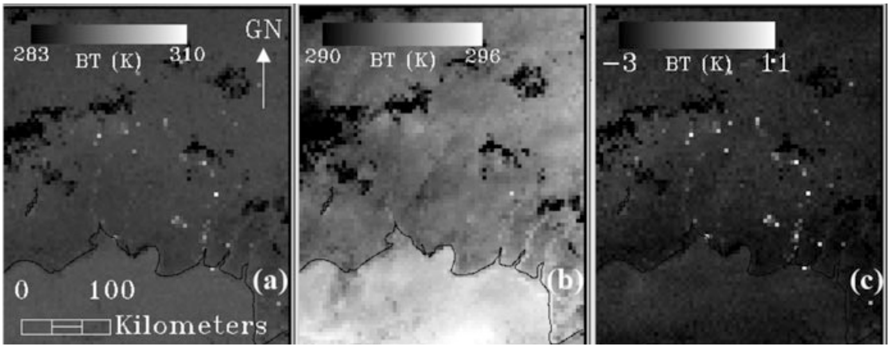

Fig. 18.3 Nighttime thermal imagery subset collected by the AVHRR sensor over southern Borneo on 24th August 1991 (coastline vector in *black*). Land clearance fires, large scale forest and peatland degradation and an El Niño related drought conspired at this time to allow large scale fires to develop across the region. AVHRR collects data in both the (**a**) MIR [3.6–3.9 μm waveband] and (**b**) LWIR atmospheric windows [in this case the 10.3–11.3 μm waveband]. Clearly at the 1.1 km nadir spatial resolution of AVHRR, the fires are not filling pixels, but rather are highly subpixel events as modeled in Fig. 18.4. The original spectral radiance measures, of the type simulated in Fig. 18.4, have here been converted to brightness temperature measures via the inverse Planck function, and a linear contrast stretch applied for display purposes. The fires affect the MIR pixel integrated brightness temperatures much more than the LWIR brightness temperatures. The image subset shown in (**c**), calculated as the difference between the MIR and LWIR brightness temperatures, therefore highlights fire affected pixels particularly well

methods, and can be made through the full depth of Earth's atmosphere, even through significant smoke (Fig. 18.3).

Of course, in contrast to the passive solar reflectance observations that are typically used to detect burn 'scars', the thermal radiation emitted by fires must (by necessity) be measured whilst combustion is actually occurring. Hence, the technique is often referred to as 'active fire' remote sensing. Taking 600 and 1000 K as representative temperatures of smoldering and flaming combustion, respectively (Kaufman et al. 1998a; Sullivan et al. 2003; Dennison et al. 2006), Fig. 18.2 indicates that in comparison to the radiant energy emitted from the ambient temperature background (~300 K), (i) the rate of thermal radiant energy release from a vegetation fire is much greater, and (ii) the peak thermal radiant energy release is at much shorter wavelengths. These two physical principles, which stem directly from Planck's Law and Wien's Displacement Law, serve as the basis for the thermal remote sensing of active fires.

The fact that actively burning fires emit IR so strongly, particularly at MIR wavelengths as demonstrated in Figs. 18.2 and 18.3, means that their identification, even from Earth orbit, can be based on relatively simple detection algorithms (see Sect. 18.3). It also means that (i) the output of such detection algorithms (such as 'hotspot' counts and fire location maps) can be rapidly delivered to users, and (ii) fires that cover only a very small fraction of the pixel area can in theory still be detected since they can significantly increase the MIR 'pixel integrated' signal (Fig. 18.3; Robinson 1991; Giglio and Justice 2003). Figure 18.4 demonstrates this

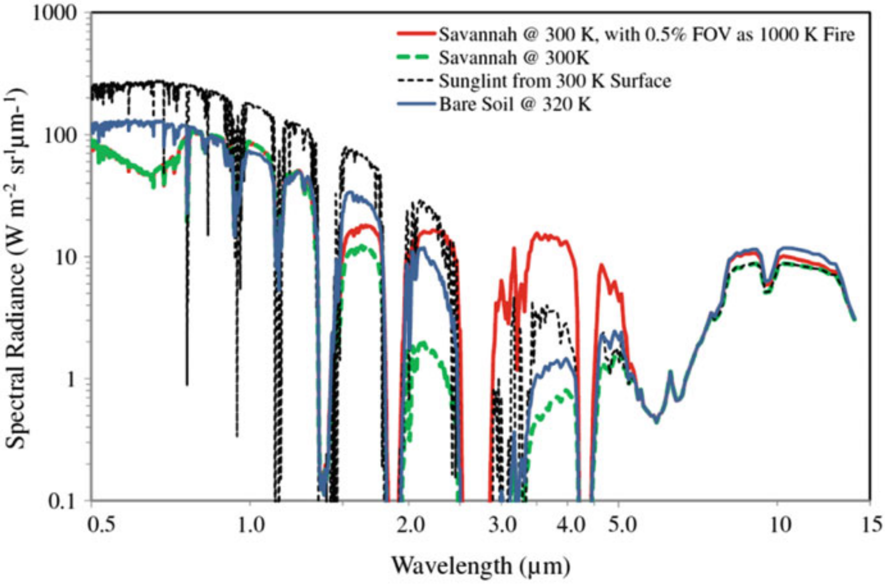

Fig. 18.4 Top-of-atmosphere spectral radiance simulated at four different target pixels (note logarithmic x and y axes) using the MODTRAN 5 radiative transfer code. Shown are simulations for a savannah surface at 300 K; the same surface but with a 1000 K fire covering 0.5 % of the ground field-of-view (*FOV*), specularly reflected sunglint from a 300 K surface; and solar-heated (320 K) bare soil. The pixel containing the sub-pixel fire shows a signal highly elevated in the MIR (3–5 μm) spectral region compared to all other targets, equivalent to a brightness temperature of around 400 K (See Wooster et al. 2012 for more detail)

principle further by simulating the spectral signature of a series of different ground targets observed from Earth orbit using the MODTRAN-5 (MODerate resolution atmospheric TRANsmission) radiative transfer code, assuming a US 1976 Standard atmosphere and rural aerosol. Whilst the savannah pixel containing a 0.5 % coverage of a 1000 K fire shows a slightly elevated signal in the LWIR (8–14 μm) compared to the non-fire savannah, it actually shows a lower signal than the 320 K solar heated bare soil. The fire pixel is, however, very well separated from all the ambient pixels in the MIR (3–5 μm), where it has a spectral radiance signal ~20× higher than the non-fire savannah pixel. However, as also illustrated, sun glints can also generate high spectral radiances in the MIR, and relatively lower spectral radiances in the LWIR, so can potentially be confused with pixels containing sub-pixel sized fires. However, sunglint pixels can be discriminated from active fire pixels using measurements in the VIS-to-NIR spectral region (0.4–1.2 μm), since highly sub-pixel fires emit insignificantly here (see Fig. 18.4).

The informative, rapid and directly useable capability to detect even very highly sub-pixel sized areas of burning vegetation has led to the widespread utilisation of active fire remote sensing over the last few decades, including from spaceborne platforms and at scales ranging from local and regional (e.g. Figs. 18.1 and 18.3) to

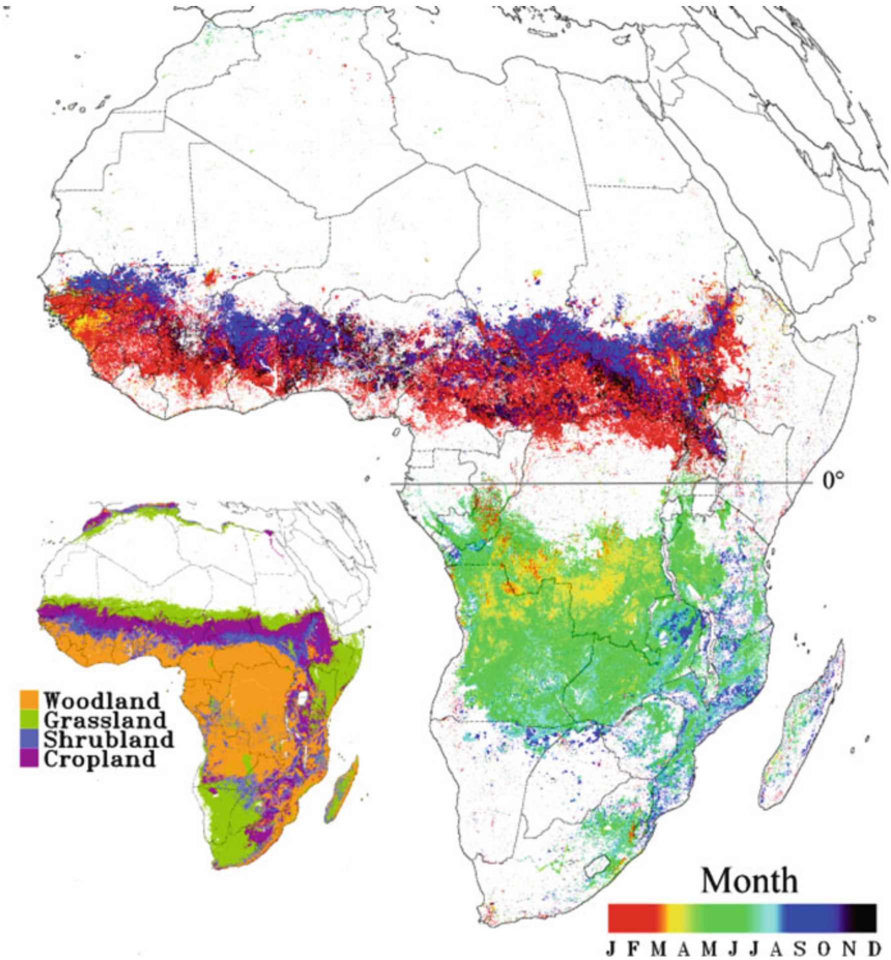

Fig. 18.5 Active fire detections made across Africa in 12 months (February 2004 to January 2005) using data from the geostationary Meteosat SEVIRI instrument. Detections are coloured by day of detection to define the different fire seasons north and south of the equator. Multiple fires in the same grid cell are given the date of the last detected fire event. Fire detections were made using the algorithm of Roberts and Wooster (2008), an adaptation of which is used to generate the near real-time Meteosat FRP (fire radiative power) Pixel products available from the EUMETSAT Land Satellite Application Facility (URL2). Inset shows African land cover aggregated into four broad classes, as derived from the Global Land Cover 2000 dataset (Mayaux et al. 2004) (Figure adapted from Roberts et al. 2009)

continental and global (e.g. Figs. 18.5 and 18.6). As just one example, the Fire Information for Resource Management System archives and distributes MODIS (Moderate Resolution Imaging Spectroradiometer) Active Fire detections and associated fire maps in near real time to many worldwide users (URL1; Davies et al. 2009). Furthermore, thermal remote sensing techniques can move beyond fire

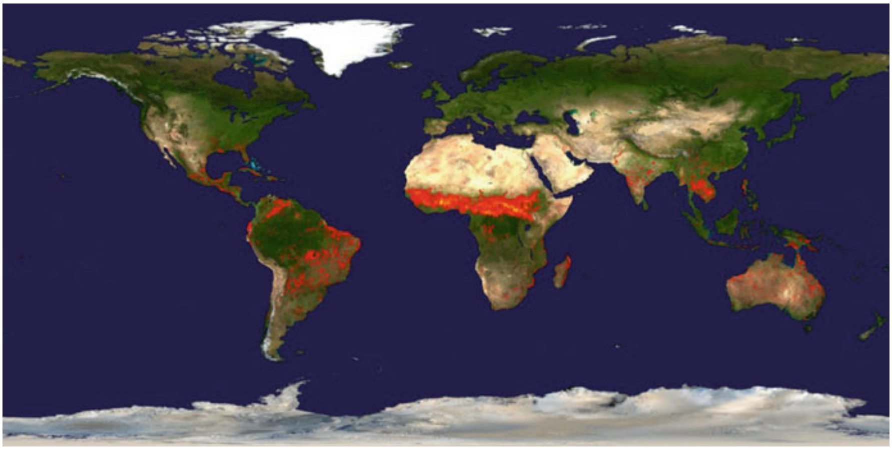

Fig. 18.6 Global active fire map based on the accumulated locations of fires detected by the MODIS instrument on board the Terra and Aqua satellites. Detections were made over a 10-day period (16–25 December 2012) using the algorithm of Giglio et al. (2003). Each *red/yellow dot* indicates a location where MODIS detected at least one fire during the compositing period. Colour ranges from *red* (low fire count) to *yellow* (high fire count). Fire map created by Jacques Descloitres. Fire detection algorithm developed by Louis Giglio. *Blue Marble* background image created by Reto Stokli. The latest near-real time image maps can be obtained via the NASA LANCE (Land and Atmosphere Near-real-time Capability for Earth Observing) system (URL3) and links therein, whilst regularly updated global active fire location data is available from MODIS via the FIRMS (Fire Information for Resource Management System) (URL1)

detection to offer more quantitative descriptions of fire's radiant energy release (Kaufman et al. 1998a; Wooster et al. 2003). Equation (18.1) indicates that the radiant energy released by a fire relates linearly to the amount of material combusted, and the amount of gas and aerosol emissions ('smoke') produced, pointing the way to the estimation of these quantities via measurement of fire-emitted electromagnetic radiation (Kaufman et al. 1998a; Wooster et al. 2005; Freeborn et al. 2008; Ichoku and Kaufman 2005; Kaiser et al. 2012; see Sect. 18.7).

Though very detailed observations of fires can be made through smoke, meteorological cloud cover remains a problem. Fortunately, the 'fire season' of most fire-affected regions generally follows dominant climatic patterns, and times of peak fire usually coincide with dryer periods with lower cloud cover (Fig. 18.5).

Furthermore, in many ecosystems the majority of the area burned in wildfires, and thus the majority of the smoke emitted, occurs in the largest few percent of fire events. Therefore, many thermal remote sensing applications need not aim to detect every single fire, but can rather focus on the more significant, larger and/or longer-lived events, which are generally the easiest to detect (Schroeder et al. 2008a). Figure 18.6 illustrates the global fire situation for a 10 day period based on data from the polar-orbiting MODIS sensors.

18.3 Methods of Active Fire Detection from Space

18.3.1 Algorithm Basics

Flaming fires emit very significantly in the shortwave infrared (SWIR) atmospheric window (1.6–2.5 μm; Figs. 18.1 and 18.2). However, as already stated, strong daytime solar reflections at these wavelengths, and the fact that many more fires burn by day than by night (Fig. 18.7), has steered the development of active fire detection towards use of the middle infrared (MIR) atmospheric window (3–5 μm). Here, levels of solar reflected radiation are lower than in the SWIR, while thermal energy emission rates from fires are very much higher than from the ambient temperature background, such that pixels containing even highly sub-pixel active fires often show up clearly in MIR imagery (Figs. 18.3 and 18.4). As a result, cooler, smoldering fires that might be almost impossible to detect in the SWIR region can still be quite clear in the MIR, and flaming fires generally show up extremely well. Many works have outlined the basis by which such 'fire pixels' can be automatically discriminated (e.g. Robinson 1991). Since at MIR wavelengths the spectral radiance (W m^{-2} sr^{-1} μm^{-1}) emitted from flaming vegetation can be up to four orders of magnitude higher than from the surrounding ambient background (Fig. 18.2), areas of combustion occupying even a very small fraction of the pixel area (e.g. 0.1–1.0 %) can result in significant increases in the pixel-integrated signal (see example in Fig. 18.4). Detection of these types of elevated MIR channel signals is therefore the basis of most active fire detection algorithms (Robinson 1991), and a review can be found in Li et al. (2002).

By day, solar-heating of bare ground and/or specularly reflected sunlight can increase MIR channel signals in non-fire pixels, potentially resulting in false positives if fire pixel detection is based on thresholding of the MIR channel pixel signals alone (Zhukov et al. 2006). Therefore, in addition to simple MIR channel signal thresholding, a series of additional spectral and/or spatial tests are generally employed to best discriminate 'true' fire from false alarms. Rather than identifying fires based on the pixel-integrated spectral radiances, such as are modeled in Fig. 18.4, most active fire detection algorithms in fact work on brightness temperature (BT) measures, which are easily calculated from the spectral radiances using the inverse Planck function (Wooster et al. 1995). Areas of solar heated vegetation, bare soil, and rock tend to exhibit quite similar brightness temperatures in the MIR and LWIR atmospheric windows (i.e. $BT_{MIR} \cong BT_{LWIR}$), but pixels containing sub-pixel sized actively burning fires can be discriminated these since the latter typically show $BT_{MIR} \gg BT_{LWIR}$ as was demonstrated in Fig. 18.3. Therefore, thresholds based on the brightness temperature difference measured between the MIR and LWIR channels is a common feature of active fire remote sensing algorithms. Although such elevated BT differences can also occur in pixels affected by sunglint (either from clouds or water bodies), it is possible to exclude such pixels since they typically show increased signals in the visible wavelength region, while active fire pixels usually do not (Fig. 18.4). Based on these basic principles,

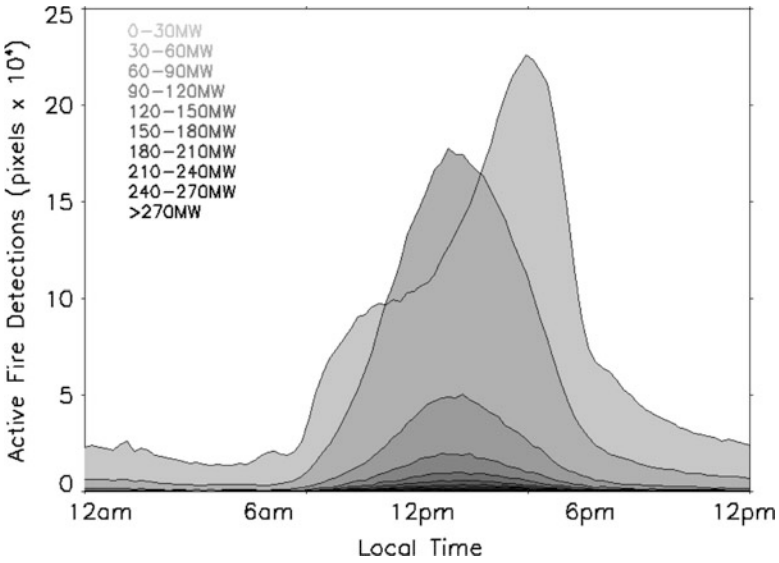

Fig. 18.7 The diurnal fire cycle in northern hemisphere Africa, based on the number of active fire detections made using data from the geostationary Meteosat SEVIRI imaging radiometer, examples of which were shown in Fig. 18.5. The fire pixel detection statistics are here shown binned into fire radiative power (FRP) bins covering 30 MW intervals (shown in various *grey shades*). FRP is a measure of the rate of release of thermal radiative energy by all fires burning within the pixel (see Sect. 18.6 of main text). Numbers of fire pixels decrease as FRP increases, which is also demonstrated in the frequency-density plots shown later in Fig. 18.14. Fire pixels at all FRP magnitudes are maximal in the early to late afternoon, which is the peak of the diurnal fire cycle in most fire affected regions

multispectral active fire detection algorithms enable the identification of even highly sub-pixel actively burning fires, while mostly avoiding false alarms (e.g. Giglio et al. 2003; Zhukov et al. 2006; Roberts and Wooster 2008).

Early active fire detection algorithms were designed for data collected in a particular geographic region and/or season, often relying on subjectively fixed detection thresholds (e.g. Flannigan and Vonder Haar 1986). Most were intended for use with data from polar orbiting satellite instruments such as the Advanced Very High Resolution Radiometer (AVHRR), which has a spatial resolution of 1.1 km at nadir or lower if the sub-sampled GAC version of the data are used (e.g. Wooster and Strub 2002). For example, Baum and Trepte (1999) classed AVHRR pixels as containing actively burning fires if they passed the following four simple tests:

$$BT_{MIR} > 314\,\mathrm{K} \tag{18.2}$$

$$BT_{MIR} - BT_{LWIR} > 10\,\mathrm{K} \tag{18.3}$$

$$BT_{LWIR}(\text{clear sky}) - BT_{LWIR} < 6\,\mathrm{K} \tag{18.4}$$

$$BT_{LWIR} < 310\,\mathrm{K} \tag{18.5}$$

Fixed-threshold approaches such as this can work well for individual scenes or time periods, but often provide poor performance during multi-regional and/or multi-seasonal analyses, and are not really appropriate for use in studies where the sensor used may change over time. In such cases, issues such as spatio-temporal changes in the ambient background thermal conditions make the use of fixed thresholds problematic (Giglio et al. 1999). This realization led to the development of so-called 'contextual' active fire detection approaches (Justice et al. 1996; Flasse and Ceccato 1996; Kaufman et al. 1998a). These approaches generally have two pathways by which pixels containing actively burning fires can be identified. The first 'fixed threshold' pathway may use a single algorithm stage, and is designed to detect pixels unambiguously containing large and/or intensely burning fires. The stage generally consists of thresholding tests akin to those in Eqs. (18.2), (18.3), (18.4), and (18.5), with fixed thresholds set sufficiently high such that in theory only pixels certain to contain fires pass the tests. The second 'contextual' pathway typically consists of two or more stages, whereby potential fire pixels (PFPs) are first identified using a fixed threshold approach based on relatively low thresholds (thus selecting many non-fire pixels as well as true fires), and then testing each PFP against the statistical properties of its immediately surrounding 'ambient background' pixels in order to confirm whether or not it is a 'true' fire pixel. The entire algorithm, incorporating the 'two pathway' approach, is generally termed a 'contextual active fire detection algorithm'.

Most current methods for identifying actively burning fires include some form of contextual approach, including the algorithms used to generate the Geostationary Operational Environmental Satellite (GEOS) Advanced Biomass Burning Algorithm (ABBA) fire products (Prins and Menzel 1992), the MODIS Active Fire and Thermal Anomaly products (Giglio et al. 2003), the BIRD Hotspot Recognition Sensor (HSRS) fire products (Zhukov et al. 2006) and the Meteosat SEVIRI fire products (Roberts and Wooster 2008). Variants of the approach exist in each algorithm, for example the algorithms developed for use with BIRD HSRS and Sentinel-3 Sea and Land Surface Temperature Radiometer (SLSTR) data first divide each scene into a set of sub-scene windows, from which obvious non-fire pixels are masked out. A set of 'background statistics' calculated from these non-fire pixels are then used to test whether the remaining pixels within the window are likely to contain active fires (Zhukov et al. 2006; Wooster et al. 2012).

Table 18.1 lists the main polar orbiting Earth Observation sensors currently used for active fire detection, including their basic spectral, spatial, and temporal specifications, and some suggestions for references where further information can be obtained. While the Defense Meteorological Satellite Program (DMSP) Operational Linescan System (OLS) does not have a dedicated MIR or LWIR spectral band for active fire detection, the low-light visible wavelength imaging capability of this sensor has long been used for active fire detection (Elvidge et al. 1996). Apart from the DMSP OLS, and the Terra Advanced Spaceborne Thermal

Table 18.1 Specifications of currently operating polar-orbiting systems commonly used for active fire detection and study

Satellite(s) sensor	Repeat cycle/equator crossing	Coverage	Spatial resolution	Example reference(s)	Example product(s)
NOAA POES AVHRR	~4× per day, local crossing times vary with satellite number	2,400 km swath, global	1.1 km at nadir	Li et al. (2000), Stroppiana et al. (2000)	Global AVHRR Active Fires (1992–93) EC JRC (bioval.jrc.ec.europa.eu)
Terra & Aqua MODIS	10:30/22:30 hrs and 01:30/13:30 hrs local time	2,340 km swath, global	1 km at nadir	Kaufman et al. (1998a), Giglio et al. (2003)	MODIS Active Fires (2000–current): NASA (reverb.echo.nasa.gov)
ERS & ENVISAT (A)ATSR	~4 overpasses/month at equator to ~12 at ±70°N/S (night)	512 km swath, global	1 km at nadir	Mota et al. (2006), Giriraj et al. (2010)	(A)ATSR World Fire Atlas (1996–current) ESA (earth.esa.int)
DMSP OLS	09:54/21:54 and 06:04/18:04 local time (night)	3,000 km swath, global	0.56 km, "smoothed" to 2.7 km	Elvidge et al. (1996)	No regular, web-based accessible global product known
Terra ASTER	Limited to a prioritized acquisition schedule	60 km swath, limited schedule	30 m	Giglio et al. (2008)	No global product
TRMM VIRS	Twice/day every other day at equator, and twice/day at temperate latitudes	720 km swath, ±40° of the equator	2.1 km at nadir	Giglio et al. (2000), Giglio (2007)	TRMM VIRS Monthly Fire Product NASA (1998–2005) (disc.sci.gsfc.nasa.gov)

Emission and Reflection Radiometer (ASTER) sensor, whose active fire detection capability is based on analysis of 30 m spatial resolution SWIR data, all other sensors listed primarily employ MIR and LWIR measurements in the active fire detection process. Furthermore, in addition to these polar orbiting instruments, there exists a strong capability to detect fires from geostationary sensors, with improved temporal resolution compared to polar-orbiting systems. Examples here include fire products created from the GOES East and West imagers (Prins and Menzel (1992, 1998, URL4), Xu et al. (2011; URL5) and from Meteosat Second Generation (MSG) (Roberts and Wooster 2008; URL2). Examples of data from the latter were shown in Fig. 18.5.

18.3.2 Further Active Fire Detection Algorithm Adaptations

In addition to the multispectral tests discussed above, several additional processing methods can be used to potentially improve active fire detection accuracy, and/or increase processing speed. For example, the aforementioned Sentinel-3 SLSTR algorithm uses the 'spatial filter' edge detection test first introduced for use with geostationary Earth observation imagery by Roberts and Wooster (2008) and then by Xu et al. (2011). The aim is to enable use of very liberal thresholds during Stage 1 of the contextual detection pathway, maximising the ability to detect small or weakly burning fires, whilst minimizing the number of non-fire PFPs passed to the 'contextual' Stage 2 due to these being relatively computationally demanding (and thus time-consuming). In order to reduce errors of omission and commission, the unique high frequency, fixed viewing geometry afforded by geostationary platforms enables further inclusion of multi-temporal tests that make use of imagery taken at different times of day. Figures 18.5 and 18.7 show examples of the broad spatial coverage, high temporal resolution data that can be gathered from use of geostationary fire detection methods, in this case applied to Meteosat SEVIRI (Roberts et al. 2009). The Advanced Biomass Burning Algorithm (ABBA) developed for use with the GOES imager (Prins and Menzel 1992) makes use of high temporal information to filter out active fire pixels detected only once at the same pixel location in any 12 h period, assuming most of these to be false alarms (Prins et al. 1998). An alternative multi-temporal approach, also developed for GOES and described by Xu et al. (2011), does not filter out such 'single pixel detects', but instead separates fires from false alarms by exploiting fluctuations in a pixel's MIR radiometric signal as a new fire ignites, intensifies, and ultimately extinguishes or propagates into a neighboring pixel.

Since meteorological clouds are generally quite opaque at IR wavelengths, and very thick smoke plumes can also be difficult to sense through, the utility of any active fire detection strategy can be thwarted under such conditions. Therefore, in an active fire remote sensing product, a pixel may be denoted as a 'non-fire pixel' due to the presence of cloud cover, rather than as the result of active fire detection testing. For this reason, a number of satellite-based active fire products also include

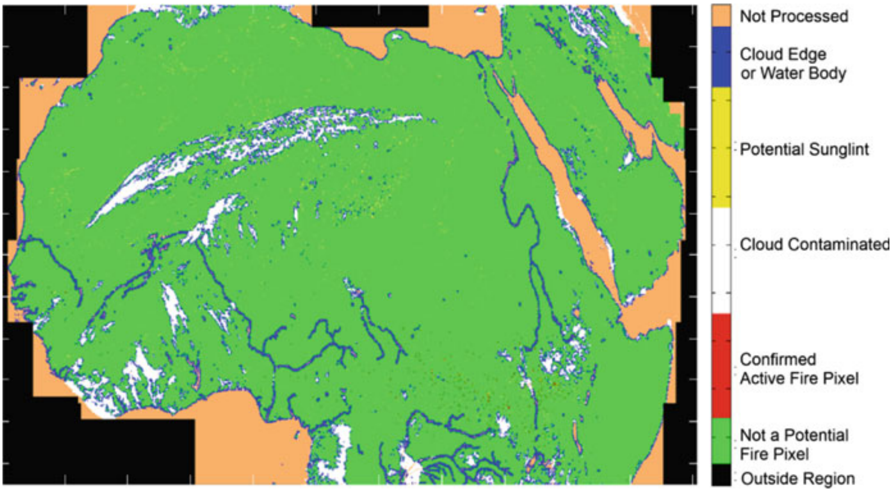

Fig. 18.8 Fire mask for North Africa down to the equator, created from Meteosat SEVIRI imagery. The mask delineates pixels which are processed by the active fire detection algorithm, and which are not (due for example to cloud cover, or to their being classified as water bodies). Other information includes which pixels are potentially contaminated by sun glint, and which are confirmed active fires. This mask forms the 'Quality Flag' component of the 'FRP Pixel product' obtainable in near real-time from the EUMETSAT Land Satellite Application Facility (URL2)

cloudiness metrics for each pixel, sometimes alongside other information such as a land/water classification and a mask of areas identified as sun glint. The MODIS Active Fire and Thermal Anomaly (MOD14/MYD14) products listed in Table 18.1 include this type of information (Giglio et al. 2003), as do the Meteosat SEVIRI FRP-PIXEL products available from the EUMETSAT (European Organisation for the Exploitation of Meteorological Satellites) Land Satellite Application Facility (URL2). An example of the latter is shown in Fig. 18.8, and some studies use this type of information to normalize active fire pixel counts for the proportion of the land surface actually viewed, for example to better compare active fire statistics across space and time (e.g. Di Bella et al. 2006) or to estimate total fire activity from the viewable fraction (e.g. Kaiser et al. 2012).

18.4 Airborne Active Fire Detection

Whilst the active fire detection capability from the low Earth orbit systems listed in Table 18.1 offers a high degree of utility and data richness, and the geostationary systems can offer an additional coarser spatial resolution but much higher temporal resolution view, satellite-based systems are still restricted in what they can provide to help analyze the type of fine scale, rapid variations in fire behavior associated with variable topography, fuel properties, and weather. Furthermore, the real or

Table 18.2 Example specifications of some of the key airborne IR sensors commonly used for active fire detection and study

Sensor	Bands	Spectral coverage	IFOV	FOV
AVIRIS	224	VIS-NIR-SWIR	1 mrad	34°
Phoenix	2	MIR-LWIR		120°
ABAS	3	NIR-MIR-LWIR	0.3 mrad 0.7 mrad	80° 19°
AIRDAS	4	VIS-SWIR MIR-LWIR	2.6 mrad	108°
AMS	12	VIS-NIR-SWIR MIR-LWIR	1.3 or 2.5 mrad	43° or 86°
FireMapper	2	LWIR	1 mrad	35°
MASTER	50	VIS-SWIR MIR-LWIR	2.5 mrad	86°
MAS (now enhanced MAS)	50	VIS-SWIR MIR-LWIR	2.5 mrad	86°

perceived delays involved in the obtaining of satellite active fire products are often cited by field personnel involved in fire management as reasons against incorporating such products into operational and strategic fire management plans (Trigg and Roy 2007). This is despite the actually quite rapid delivery of EO products such as those supported by, for example, FIRMS (URL1; Davies et al. 2009), GOES ABBA (URL4), and the EUMETSAT Land Satellite Application Facility (URL2). Nevertheless, the fact that airborne systems can operate near continuously as needed (albeit at a logistical and financial cost), and can quite easily provide meter or even sub-meter spatial resolution imagery, at repetition frequencies as high as every few minutes or even better, means they are highly capable of supporting fire management operations. Table 18.2 details some of the commonly used airborne remote sensing systems related to active fire observations, and although issues of geo-referencing and calibration typically become more significant hurdles than with satellite data products, there are airborne systems that can directly deliver quantitatively useful datasets rapidly to users on the ground. Airborne thermal remote sensing therefore provides a very useful tool with regard to active fires, and its exploitation has followed two main paths. Firstly an 'operational' agenda for direct use in fire suppression and post-fire rehabilitation operations, and secondly a research agenda related in some cases to future satellite instrument or algorithm development.

18.4.1 Operational Airborne Thermal Fire Mapping

Thermal imaging systems have had a long and widespread use in patrol aircraft, aiding spotters looking for new forest fires. Many airborne IR systems are also used as decision support tools. Though costly to acquire and deploy operationally, the use of IR imaging in this way can help minimize ineffective fire suppression strategies. This is particularly the case during prolonged responses to large or contentious wildfires (often termed 'project fires', 'siege campaigns', or in the United States as 'Type 1' fires), where the Incident Commander is responsible not only for effecting fire suppression, but also for defending human, economic and cultural values. This task can require a great deal of information to affect successfully, including on both current and forecast fire behavior. Such 'project fires' often take place in situations involving severe fire behavior and significant risk to human, economic and/or cultural values, resulting in suppression costs often exceeding US $1 million per day.

During a large fire event, the suppression tactics employed depend strongly on knowledge of a fire's current behavior. However, thick smoke columns, heterogeneous fuel structures, and dense canopy cover often conspire to make assessment of the fire situation difficult with the human eye, even from an airborne vantage point. Tasks such as differentiating the intensity of surface fuel combustion within a single fire perimeter, or locating spot fires outside of the perimeter, can become very difficult. In such cases, the enhanced view of the fire provided by airborne thermal imaging, which as mentioned above can penetrate smoke, and to some extent also vegetation cover, allows for a much better assessment of current fire behavior (see example in Fig. 19.9). This capability helps Incident Commanders evaluate the success of ongoing suppression efforts, allowing them to make better informed tactical decisions regarding the distribution of manpower and other resources. The ability to provide clearer views of the fire situation than can be gained with unaided eyesight or optical wavelength imaging is also the operational driver for the installation of thermal imagers onboard fixed wing tanker aircraft. This allows pilots to acquire suitable targets for water or flame retardant drops, even through smoke columns. In the later stages of fire suppression, ground personnel are also sometimes equipped with handheld thermal imagers, particularly to help locate areas of smoldering combustion below layers of ash, and thus ensure that more thorough suppression is conducted and new fires cannot start from still smoldering areas of fuel.

Much of the early development work regarding the thermal imaging of fires from aircraft was conducted by the United States Forest Service (USFS). USFS projects like FIRESCAN had been using thermal sensors for 'wildland' fire detection, monitoring and decision support since the early 1960s (Warren and Celarier 1991; Lentile et al. 2006). According to Warren (1992), the focus was on airborne systems even in the early days, with little or no use made of the type of 'fixed area' thermal scanners used in several European countries at the time. Such tower mounted systems usually included both a thermal and optical imaging capability, which were exploited by an operator to perform scans of all or part of the full 360° view around the installation. Thermal imaging from aircraft allowed larger areas to be rapidly surveyed, and early USFS studies were based on IR line scanners, often modified militarily equipment operating in both the longwave IR (8–14 μm using a HgGe detector) and middle IR (3–5 μm using an InSb detector) spectral regions. These systems were considered to deliver data with acceptable accuracy at the time, could image in excess of 2,500 $km^2\ h^{-1}$, and were able to detect very small fires. Particularly so when the dual waveband systems were used, due to the aforementioned increased hotspot sensitivity and algorithm performance when exploiting MIR data (Sect. 18.3; Hirsch and Madden 1969; Warren and Celarier 1991). When 'handheld' 'Forward Looking Infrared' (FLIR) thermal imaging systems first became commercially available in the late 1970s and 1980s, they also became part of the airborne fire detection arsenal. The small size of FLIR systems, and (unlike line scanners) their lack of a requirement for aircraft forward motion to build a 2D image, meant they were particularly well suited to deployment on helicopters, which due to their ability to hover, takeoff and land in small spaces, and carry a variety of payloads, are widely used in fire management and suppression operations (Warren and Celarier 1991). The helicopter-mounted FLIR imagers often provided much more detail than line scanning systems, albeit generally over smaller areas, and due to their high spatial resolution it was not particularly necessary to have a system that operated at MIR wavelengths since in many cases pixels were completely filled by fire.

From 1985, the US Forest Service 'Fire Mouse Trap' (Flying Infrared Enhanced Maneuverable Operational User Simple Electronic Tactical Reconnaissance and Patrol) system attempted to exploit FLIR technology alongside LORAN navigation to deliver a semi-near real time forest fire mapping capability from helicopters and small fixed wing aircraft (Dipert and Warren 1988; Warren and Celarier 1991). Around the same time, the United States National Aeronautics and Space Administration's Jet Propulsion Laboratory (NASA-JPL) developed an airborne fire mapping program called the Fire Logistics Airborne Mapping Equipment (FLAME) project. The FLAME instrument was a dual-band (MIR and LWIR) IR-scanner system, apparently able to detect 1 m^2 fires from 3.5 km altitude (Nichols et al. 1989). The subsequent 'Firefly' system exploited same two wavelengths, and became the first digital fire detection and monitoring system used by the United States National Interagency Fire Center, with data processed onboard aircraft and transmitted by way of satellite to the Incident Command Post (Warren and Celarier 1991; USFS 2012). FLAME was further upgraded in 1998 and repackaged as the Phoenix system, which also provided digital imagery output. More recently, the US Wildfire Airborne Sensor Program (WASP) has been developed using three commercially available FLIR-style cameras operating at 1.3, 3.25, and 8.6 μm (Li et al. 2002). In Canada, systems such as the Airborne Wildfire Intelligence System (AWIS) and the ITRES TABI-1800 (Thermal Broad-band Imager) provide similar support to operational fire management (Fig. 18.9).

In addition to its role in fire management and response, an important additional remit for airborne thermal remote sensing in relation to fire has been to assist national agencies and aerospace organizations in the testing of new instrument types, the evaluation of new algorithms, and the calibration of satellite-based sensors. Instruments often more capable than those typically deployed on fires on an operational basis are often used for these applications. Examples are the Airborne Visible/Infrared Imaging Spectrometer (AVIRIS) measuring from 0.4 to 2.5 μm in 224 contiguous spectral bands, the FireMapper IR imaging radiometer (Riggan and Tissell 2009), and the MODIS Airborne Simulator (MAS) (Green 1996; Hook et al. 2001). MAS for example is a scanning imaging spectro-radiometer which measures

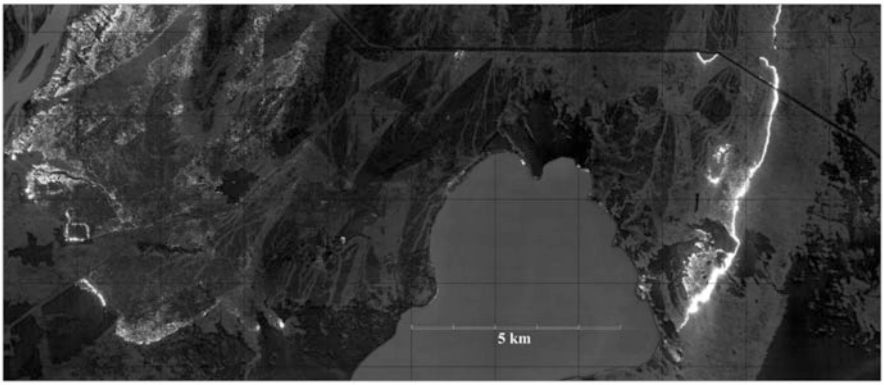

Fig. 18.9 Geocoded thermal imagery produced during a Alberta Environment and Sustainable Resource Development (*ESRD*) response to a 2011 Northern Alberta wildfire, where active fire fronts and residual hot-spots are evident as white pixels. The image was acquired using the ITRES Thermal Airborne Broadband Imager (TABI-1800), which has 1800 across-track pixels and provides MIR data to produce ortho-mosaic thermal maps in the 3.7–4.8 μm wavelength range (URL5). Vector data products of active fire fronts, hot-spots, and fire perimeters can be extracted from the imagery and used along with the thermal map to support fire suppression activities. The high temperature sensitivity of the TABI-1800 (NEdT < 30mK) allows for discrimination of subtle thermal details in addition to the highly radiant fire pixels (Image courtesy of Alberta ESRD). Image courtesy of ITRES (URL6)

reflected solar and emitted thermal radiation in 50 narrowband channels between 0.55 and 14.2 μm. At nadir it delivers 50 m spatial resolution data from the NASA ER-2 aircraft flying at 20 km altitude. An evolution of MAS is the MASTER MODIS/ASTER airborne simulator, developed firstly to support ASTER data validation and secondly as a back-up instrument for MAS (Hook et al. 2001). MAS was deployed during the Southern African Regional Science Initiative (SAFARI-2000), which conducted prescribed burns coincident with overpasses of the then recently launched EOS (Earth Observing System) Terra satellite, in part to help validate the MODIS active fire detection algorithms (Swap et al. 2002).

18.4.2 Unmanned Aerial Vehicles

There are limitations to the use of airborne thermal imaging in wildfire activities, often related to the high operational costs involved, and to the risks to aircraft and crews when flying in potentially dangerous low visibility/high turbulence situations close to fires and/or smoke columns. To try to overcome some of these issues, Unmanned Aerial Vehicles (UAVs) equipped with thermal imaging capabilities can be exploited. In the mid-2000s, the Altair-FIRE project (First Response Experiment) was amongst the first efforts aimed at demonstrating the utility of integrating UAV capabilities, advanced thermal imaging, cost-effective telemetry and (semi-) automated image geo-rectification systems (Ambrosia et al. 1994; Wegener et al.

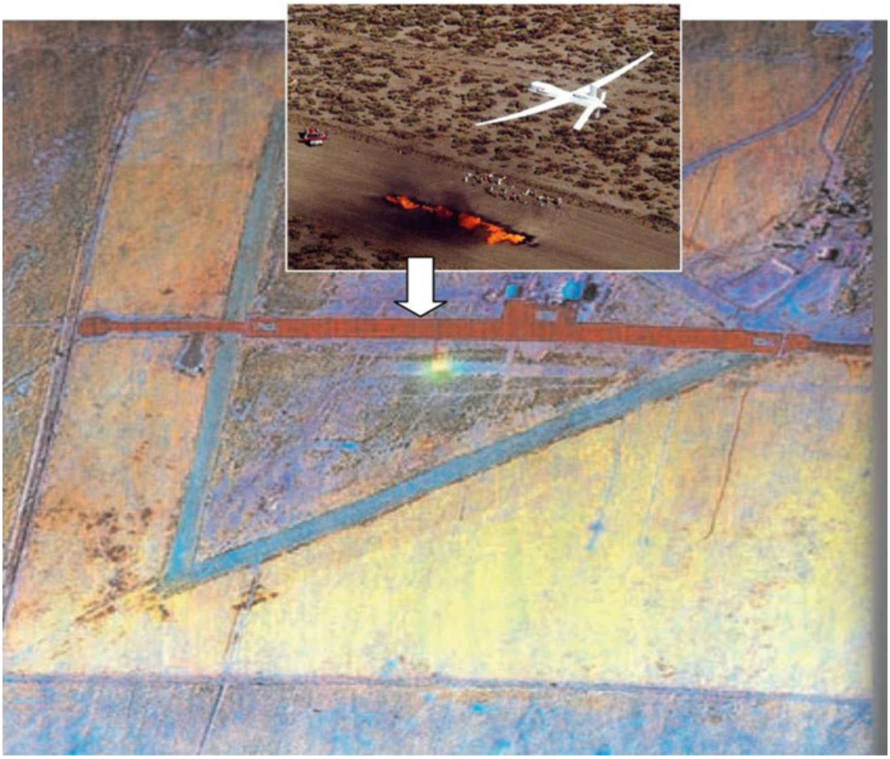

Fig. 18.10 The FiRE demonstration controlled burn conducted at El Mirage, California on 6th September 2001 (Lat 34° 37.4′, Lon −117° 36.2). The infrared colour composite collected by the ALTUS II in flight at ~945 m altitude highlights the highly radiant location of the fire, with a photographic view of the scene taken from a higher altitude aircraft shown in the *inset*

2002; Ambrosia et al. 2003). Mounted on an Altair platform, a modified version of the military '*Predator*' *UAV,* the payload consisted of a multispectral imager having a visible-to-thermal imaging capability (Fig. 18.10). In parallel, studies such as Merino et al. (2006) have tested the capability of much lower cost civilian UAVs and small micro-bolometer based LWIR cameras for the detection, monitoring, and measurement of forest fire targets.

18.5 Thermal Imagery Contributions to Burned Area Mapping

While the focus of the spaceborne and airborne thermal remote sensing methods discussed thus far has been on the detection of actively burning fires, such measurement capabilities also have some relevance to the identification and mapping of burned areas. This has often been simply through use of active fire detections to gauge the ultimate size of the fire-affected area, generally via some form of empirical relationship linking the number of active fire detections to the size of the area burned (e.g. Giglio et al. 2005). Since fire behaviour varies greatly between environments, such associations require careful testing and calibration. Reported slopes of the linear relationships linking the two metrics ranged in the global study of Giglio et al. (2005) between 0.29 km^2 of burned area per active fire pixel in southern-hemisphere South America, to 6.6 km^2 of burned area per active fire pixel in Central Asia. Once such relationships are established for the areas of interest, the types of long term active fire detection record available from MODIS, TRMM VIRS (Tropical Rainfall Measuring Mission, Visible and Infrared Scanner) and (A) ATSR ((Advanced) Along Track Scanning Radiometer) can be used to estimate burned area trends, provided of course that the active fire products are appropriately inter-calibrated for differences in sensor spatial resolution (and thus minimum active fire size), satellite overpass time, and image repetition frequency.

Until the recent version 3 of the widely-used Global Fire Emissions Database (GFED; Van der Werf et al. 2010), this 'hotspot counting' approach to burned area estimation based on active fire detections (Giglio et al. 2006) actually provided the vast majority of the burned area estimates used within GFED, proving its utility at a time when global burned area datasets based on spectral reflectance measurements were still largely at the development and testing stage. The most commonly used wavelengths for burned area mapping reside within the near-infrared (~0.8–1.2 μm) and shortwave infrared (~1.6–2.2 μm) spectral regions, where changes in vegetation cover and of the proportion of bare soil and charred surfaces have significant impact on reflectances. Burning of less than half of the pixel can be detected by such methods (Pereira et al. 1997; Smith et al. 2007), which while far less sensitive than active fire detection methods is still a very useable change detection threshold. The types of surface spectral reflectance change seen on burning are also often accompanied by changes in the emitted spectral radiance, and thus in the apparent brightness temperature (Fig. 18.11; Trigg and Flasse 2000; Smith et al. 2007). Such thermal changes result, for example, from the albedo decreases that come from the presence of charred surfaces, to the increased cover of exposed soils, from evapotranspiration decreases due to stress or loss of live vegetation, and from the presence of still smouldering or glowing combustion (Eva and Lambin 1998; Smith and Wooster 2005). LWIR observations are therefore sometimes used to attempt performance enhancement of burned area mapping algorithms. When mapping fire affected areas in Central Africa from ERS-1 satellites Along Track Scanning Radiometer (ATSR), Eva and Lambin (1998) noted that upon burning many pixels exhibited a sharp fall in SWIR spectral reflectance, and a simultaneous increase in LWIR brightness temperature. This was exploited to map burn scars across the Central African Republic, and without the inclusion of the LWIR data to expand the information beyond the single ATSR solar reflected (1.6 μm) waveband it is likely that classification accuracies would have been reduced. Despite this success however, most approaches attempting to incorporate both emitted and reflected spectral radiance data in a single 'burned area mapping' index have shown mixed results (e.g. Holden et al. 2005; Smith et al. 2007), and widespread adoption of the approach has not occurred. This is in part because the temperature

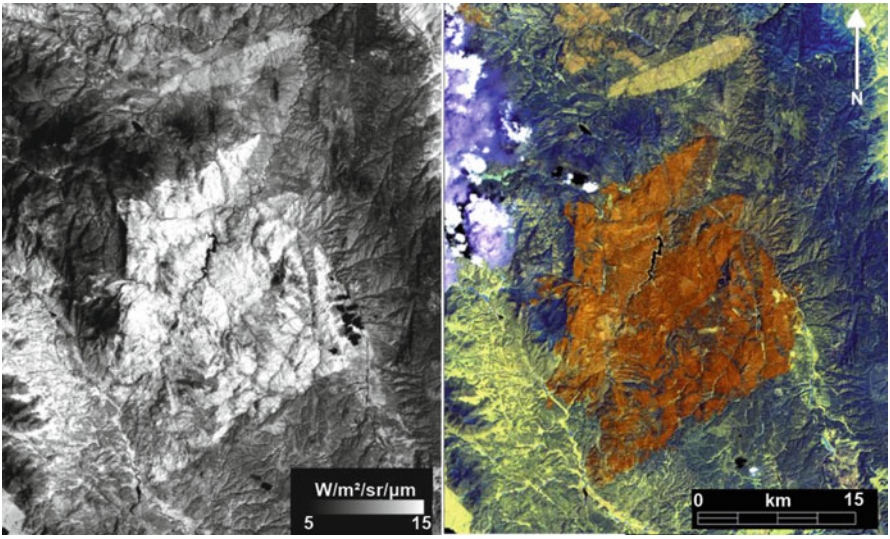

Fig. 18.11 2002 Landsat ETM+ imagery of the 559 km^2 Hayman Fire (Colorado, USA; Lat 39° 10.0′, Lon −105° 15.0′). At right is a false color composite (RGB = ETM+ bands 7, 5, 4), where exposed soil and charred surfaces appear as a *reddish colour*, and areas of unburned vegetation appear *blue*. The *right image* depicts the low-gain ETM+ band 6 LWIR spectral radiance data of the same area in a *greyscale* rendition. This indicates the burned area to have generally higher spectral radiances (warmer). However, careful interpretation of such thermal data is necessary, since areas of exposed soil (*scene bottom left*) and forest clear cuts (*scene top*) also show signs of being warmer than the vegetated areas

of post-fire surfaces is controlled not only by land cover characteristics, but also by processes unrelated to vegetation fires (e.g. other landcover properties, solar insolation and cloudiness variations; see Fig. 18.11). Also, VIS-SWIR wavelength data are often available from spaceborne sensors at a much higher spatial resolution than are the accompanying thermal imagery (e.g. MODIS' 250 m/500 m optical bands, compared to the matching 1 km thermal bands; and Landsat 7 ETM's 30 m optical bands compared to the 60 m LWIR band), making the merging of the thermal and optical wavelength imagery a less attractive prospect.

Another avenue of investigation aiming to exploit thermal measurements in burned area mapping applications has been to separate the daytime MIR spectral radiance signal into its separate solar reflected and thermally emitted contributions. This aims to exploit the perceived strong sensitivity of the reflected component to changes in certain surface characteristics, including vegetation moisture (Boyd and Petitcolin 2004). Petitcolni and Vermote (2002) detail one way to attempt this separation, based on careful atmospheric correction and the use of the Temperature Independent Spectral Indices of Emissivity (TISIE) defined by Becker and Li (1990). The resulting MIR spectral reflectance measures can, for example, be used in place of VIS wavelength data in various types of vegetation index (Kaufman and Remer 1994; Barbosa et al. 1999), and under certain conditions this has been shown to add value when attempting to discriminate burned and unburned pixels (Libonati et al. 2009).

In terms of approaches to exploiting thermal band data in burned area (BA) mapping algorithms, probably the most successful has been the inclusion of active fire detections into burned area data processing chains. Specifically, the locations of detected active fire pixels (made using the types thermally-based algorithms covered in Sect. 18.3) can very usefully act as ‘seed locations’ for optical waveband change detection methods aimed at identifying newly burned areas from optical wavelength data. Among the earliest examples is the Hotspot And NDVI Differencing Synergy (HANDS) algorithm, used to map burned areas across the Canadian boreal forest (Fraser et al. 2000). More recently, Giglio et al. (2009) utilised the technique to produce a global, multi-year burned area product from the 10+ year MODIS data record, a product which is now used as the primary burned area dataset within version 3 of the Global Fire Emissions Database (GFED; Van der Werf et al. 2010).

18.6 Fire Characterization

In addition detecting active fire pixels and contributing to the mapping of post-fire burned area, thermal IR remote sensing has a strong part to play in the characterisation of fire properties, for example the temperature and area covered by the active fire, and its rate of radiative energy emission.

18.6.1 Fire Radiative Power and Fire Radiative Energy

The complete combustion of a fixed amount of biomass releases an approximately fixed amount of thermal energy (the so-called fuel heat yield discussed in Sect. 18.2 and defined by e.g. Byram 1959 and Pyne 1984). Assuming the fraction released as radiant energy does not vary too much, then remotely sensed measurements of emitted IR radiation hold strong potential to be used to ‘back calculate’ the amount of fuel that was burned to produce that energy (Kaufman et al. 1998a; Wooster et al. 2005).

Initial attempts to use thermal remote sensing to quantify total energy emission from open vegetation fires were largely based on airborne imaging of fire spread rates. For example, Budd et al. (1997) used airborne IR data to map fire perimeters at 6–7 min intervals over a series of experimental bushfires in Australian Eucalypt. By inserting the derived rate of spread and pre-burn fuel load into the formula for Byram’s (1959) fireline intensity, it was estimated that peak head fire intensity for most fires (averaged over 6 min) exceeded 1000 kW per meter of the fire front (kW m^{-1}), and ranged as high as 3,280 kW m^{-1}. Assuming a fuel heat yield of around 18 MJ kg^{-1} discussed in Sect. 18.2, these figures equate to fuel consumption rates exceeding 3 kg min^{-1} per meter of fireline length. At a similar time, Kaufman et al. (1998a) proposed estimating the rate of radiant energy release from burning vegetation fires more directly, via direct quantitative analysis of the thermally radiant signals themselves. MODIS Airborne Simulator (MAS) was used, and the target was Brazilian cerrado fires, with the 'radiative energy release rate' metric defined by Kaufman et al. (1998a) (now usually termed 'fire radiative power', FRP) calculated via an empirical relation based on MIR brightness temperature (BT_{MIR}) measurements (Eq. 18.6). This equation has subsequently been used to generate the FRP information stored within the MODIS Active Fire Products (Giglio 2010):

$$FRP = 4.34 \cdot 10^{-19} A_{sampl} \sum \left(BT_{MIR}^{8} - BT_{MIR,bg}^{8} \right) \tag{18.6}$$

where BT_{MIR} and $BT_{MIR,bg}$ are the MIR brightness temperature (K) of the fire pixel and surrounding ambient temperature background pixels respectively, and A_{sampl} is the MODIS ground pixel area (km^2). Note that pixel area did not appear in the original formulation of Kaufman et al. (1998a), so earlier versions of the MODIS Active Fire Products (Collection 4 and previous) delivered FRP data in units of $W\ m^{-2}$ for any pixel location in the swath. However, the most recent version of the MODIS Active Fire Products (Collection 5 onwards) accounts for the change in pixel area across the MODIS swath, and so provides FRP data directly in MW per pixel (Giglio 2010)

Equation (18.6) was derived specifically for the spectral and spatial characteristics of MODIS, and the coefficients were optimized for the retrieval of FRP from fire pixels with a maximum BT_{MIR} of ~450–500 K (which represents the approximate saturation temperature of the MODIS' 3.95 μm 'fire' channel [band 21]). When applied to much higher spatial resolution imagery, where fire often fills a greater pixel proportion and BT_{MIR} values can be much higher than for MODIS, the coefficients in Eq. (18.6) are no longer appropriate. In part to counteract this, Wooster et al. (2003, 2005) derived an alternative approach to estimating FRP, approximating the Planck function with a simple power law and using this to linearly relate FRP to the fire's emitted MIR spectral radiance (Wooster et al. 2003):

$$FRP = \frac{A_{sampl}.\sigma.\varepsilon}{a.\varepsilon_{MIR}} \left(L_{MIR} - L_{MIR,bg} \right) \tag{18.7}$$

where σ is the Stefan-Boltzmann constant ($5.67 \times 10^{-8}\ J\ s^{-1}\ m^{-2}\ K^{-4}$) and ε and ε_{MIR} are the broadband and MIR spectral emissivities respectively (which cancel if the fire can be considered a greybody or blackbody, which is the commonly assumed case). $L_{MIR,}$ is the MIR spectral radiance of the fire pixel, $L_{MIR,bg}$ is the MIR spectral radiance of the ambient background (both in units $W\ m^{-2}\ sr^{-1}\ \mu m^{-1}$), and a [$W\ m^{-2}\ sr^{-1}\ \mu m^{-1}\ K^{-4}$] is dependent upon the sensor spectral response (see Wooster et al. (2005) for a full derivation).

Using multiple overpasses of fires by MAS in the Brazilian cerrado, Kaufman et al. (1998a) successfully related the detected FRP at each timestep to the rate of increase of burned area. The coefficient of determination (r^2) between the time

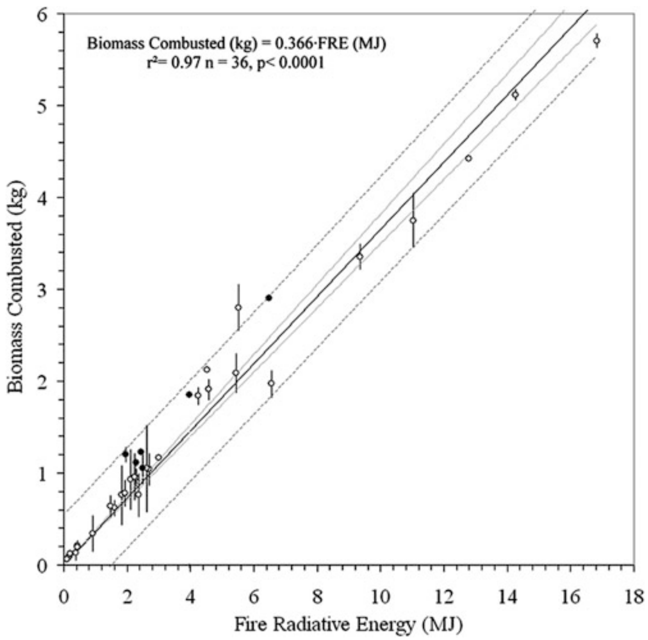

Fig. 18.12 Linear relationship between fuel consumption and Fire Radiative Energy (*FRE*, J). FRE is the temporal integral of the fires radiative power output (FRP, MW) over the fires lifetime. *Open circles* represent herbaceous fuel, and *closed circles* are woody fuel. Results taken from laboratory scale fire experiment detailed in Wooster et al. (2005). The 'combustion factor' C relating these two measures is calculated as 0.366 (kg MJ^{-1})

integrated FRP and the change in burn scar size over the same period was 0.94, significantly stronger than the $r^2 = 0.74$ relationship between the number of active fire pixels integrated over the same period and the change in burn scar size. This improvement helps indicate the additional value of quantitative thermal analyses of active fire pixels, and specifically the FRP metric, beyond simple counting of numbers of 'hotspot' pixels. The assertion of Kaufman et al. (1998a) that FRP could be directly related to fuel consumption and smoke production was later experimentally tested by Wooster et al. (2005) and Freeborn et al. (2008) under laboratory conditions. Handheld thermal imaging cameras were used to collect MIR data at a sample rate of one frame per second, and estimates of FRP derived using Eq. (18.7) were temporally integrated over the lifetime of each fire to calculate Fire Radiative Energy (FRE, MJ). The FRE was found to be very well related to the fuel biomass burned, and the slope of the linear best fit relationship between FRE and fuel burned was termed the 'combustion factor' C (kg MJ^{-1}) (Fig. 18.12).

Whilst integrating time-series measurements of FRP to yield FRE is tractable at higher imaging frequencies (e.g. the 1 Hz or better available with ground-based thermal imaging systems, or the few minutes available from repeated aircraft overpasses), retrieving FRE from sequential satellite images can become problematic since assumptions must be made about the temporal trajectory of fire behavior

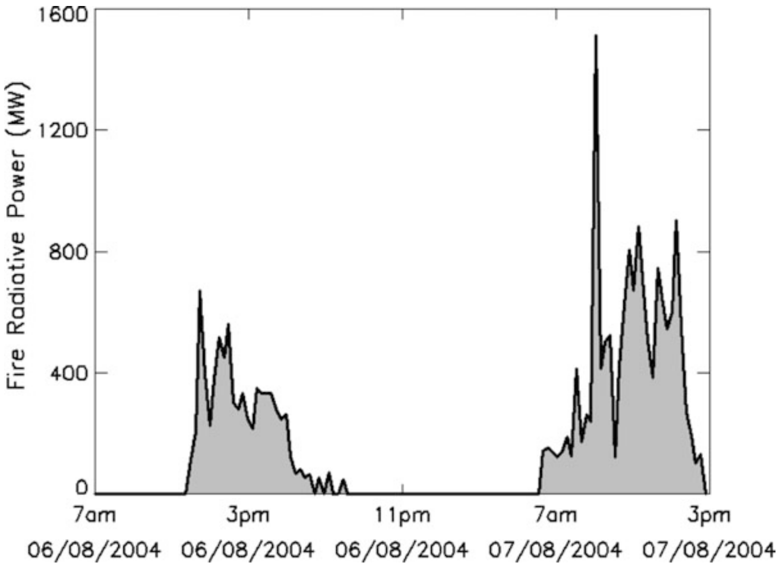

Fig. 18.13 Time-series of fire radiative power (FRP) observations made using the geostationary Meteosat SEVIRI instrument over a single fire that burned on 6–7 August 2004 in an area of grassland in northern Botswana (26.12° E, 18.28° S). SEVIRI FRP observations are available every 15 min, and for this fire there was minimal cloud cover to obstruct the surface from view during the entire measurement period. All detected active fire pixels at each imaging slot had their FRP calculated using Eq. (18.7), and the total FRP for that time slot calculated via summation of the individual per-pixel values. The typically strong fire diurnal cycle results in this case with the fire falling below SEVIRI's active fire pixel detection threshold at night, only to be re-detected the next day. The total FRE for the fire is calculated from temporal integration of the individual FRP records for the fire made at each 15 min time-slot, and equates to 12×10^6 MJ. Using these data in Eq. (18.10) and applying the 'combustion factor' (C, kg MJ^{-1}) from Fig. 18.12, this FRE equates to ~4,400 ton of dry biomass. The SEVIRI FRP product is operationally available from the EUMETSAT Land Satellite Application Facility (URL2)

based on often prolonged, uneven, and temporally undersampled observation times (Freeborn et al. 2009). Hence, geostationary satellites become attractive since they offer the highest sampling rates available from Earth orbit and are thus able to take data semi-continuously across the full diurnal cycle (Fig. 18.7).

18.6.2 Fire Diurnal Fire Cycle and Geostationary FRP Observations

Geostationary active fire observations can provide unprecedented temporal detail from high Earth orbit (Fig. 18.13). Such data show vegetation fires undergoing characteristic changes in size and/or intensity that are reflected in the FRP time-series. These variations often correlate with the metrological diurnal cycle of relative humidity, air temperature and wind, leading to the typical fire diurnal cycle seen in Fig. 18.7. More detailed analysis of FRP data returned from analysis

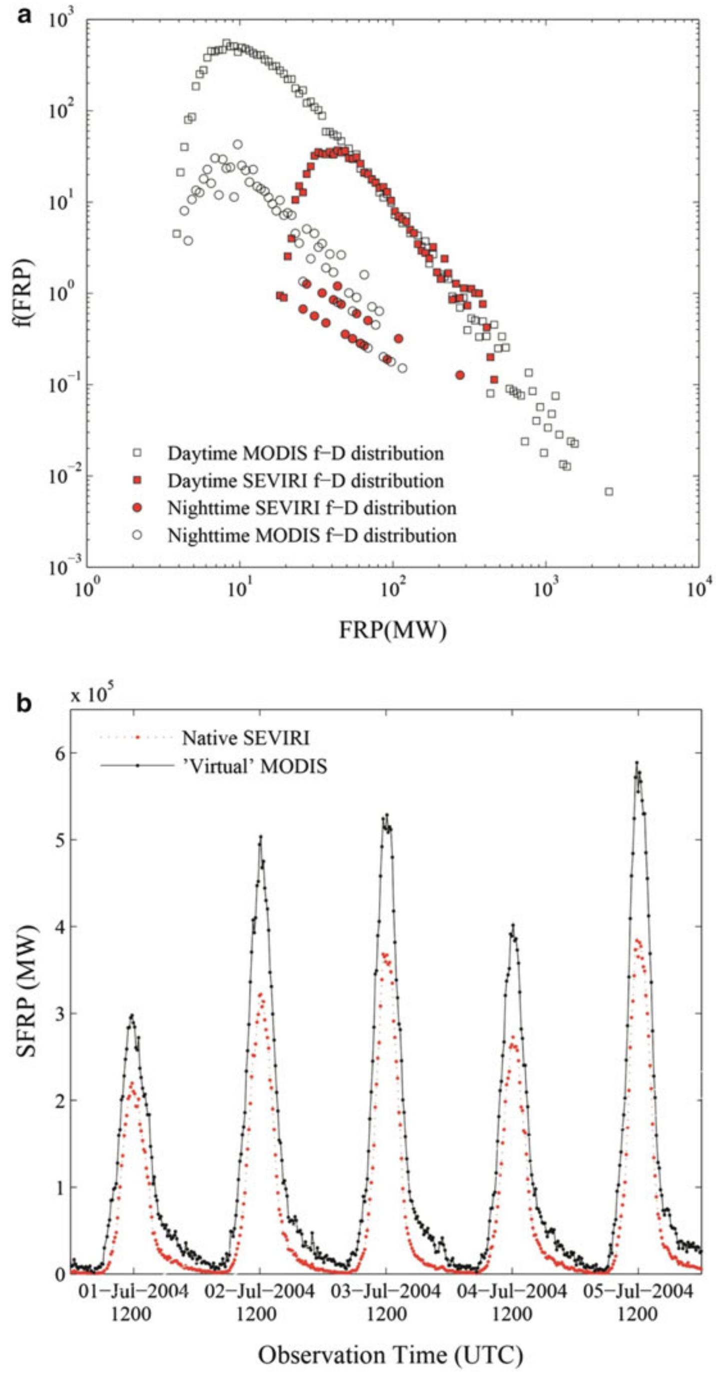

Fig. 18.14 (**a**) Fire radiative power (FRP) data of Africa, collected by the polar orbiting MODIS and geostationary SEVIRI instruments. (a) Day and night frequency density distributions of FRP for collocated fire pixels detected at the same time by SEVIRI and MODIS. Both sensors record

of Meteosat SEVIRI imagery by Roberts et al. (2009) illustrated the somewhat skewed distribution of the African fire diurnal cycle. The highest FRP fire pixels appear to occur most frequently at the peak of the diurnal fire cycle, ~14:00 hrs local time, and progression in fire activity throughout the afternoon and into the evening is characterized by a greater proportion of lower FRP fire pixels.

However, the larger pixels sizes typically available from geostationary orbit do offer some limitations, and when polar orbiting and geostationary systems view a fire affected area at the same time, the latter typically fail to detect a greater proportion of the true fire activity (Freeborn et al. 2009). Since lower FRP fires are generally more frequent than high FRP fires (Fig. 18.14a), the omission of the lowest FRP fire pixels may result in a somewhat altered apparent fire diurnal cycle, and a spatio-temporal bias in both the FRP and FRE records. To attempt to account for such biases, Freeborn et al. (2009) combined spatially and temporally concurrent geostationary (Meteosat SEVIRI) and polar orbiting (Aqua and Terra MODIS) observations, to estimate the FRP that would be derived from a MODIS-like sensor operating at the temporal resolution of SEVIRI. Figure 18.14b indicates that this 'virtual MODIS' FRP record lies consistently above that of the native SEVIRI sensor, reflecting the fact that, when viewing the same area at the same time, MODIS-type instruments generally detect a more complete record of regional fire activity than do geostationary sensors. However, in reality polar orbiters only provide such data at best a few times per day at most locations.

An alternative approach to bias correction was taken by Roberts et al. (2011), who attempted to blend geostationary FRP data with the types of burned area information commonly derived from optical remote sensing (Fig. 18.15).

The aim was again to adjust the measurement record for the presence of non-detected active fires, which remained undetected either due to their low size and FRP, or because of near continuous cloud cover while they were burning. Figure 18.15 displays the results of this 'blending' approach, indicating that this methodology provides fuel consumption estimates across Africa closer to those presented in version 3 of the GFED database than are the estimates derived from the geostationary FRE record alone. A related integrating approach based on MODIS-derived FRP and burned area data had been previously explored by Boschetti and

Fig. 18.14 (continued) fewer fire pixels at night due to the strong fire diurnal cycle (see Figs. 18.7 and 18.13), and distributions suffer from left-hand truncation due to the inability to identify a substantial proportion of the (very frequent) smaller and/or less intensely burning fires. This truncation appears at a higher FRP threshold for SEVIRI since the SEVIRI ground pixel area is ~10× that of MODIS at nadir, and the FRP detection limit is directly related to pixel area. Note the distributions also suffer from (more limited) right-hand truncation due to sensor saturation over some of the largest/highest intensity fires. (**b**) Fire radiative power (*FRP*) data of Africa, collected by the polar orbiting MODIS and geostationary SEVIRI instruments. (b) Direct comparison between summed FRP actually measured by SEVIRI for a 5° grid cell over Africa every 15-min, and the higher values which would be measured by MODIS over the same area if it could operate at the same temporal resolution as SEVIRI (Adapted from Freeborn et al. 2009)

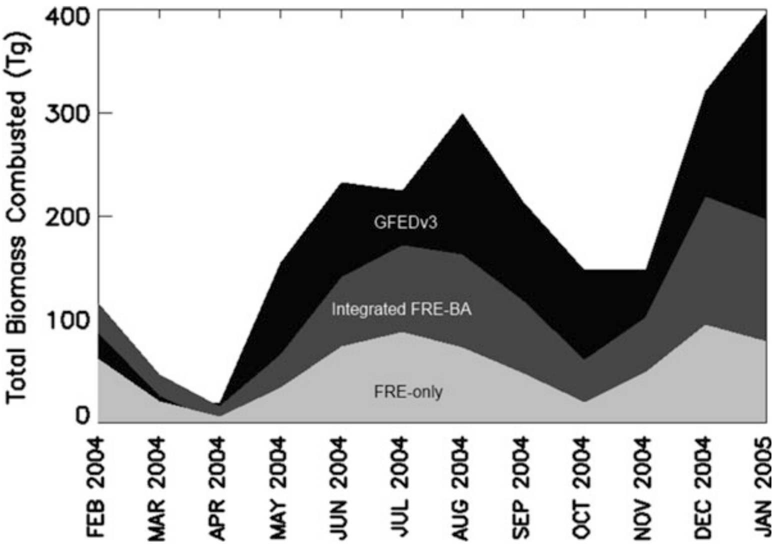

Fig. 18.15 Monthly total biomass consumption in fires across the African continent, calculated from three different methods. The 'FRE-only' approach uses the SEVIRI FRP product (Roberts and Wooster 2008) to calculate the total Fire Radiative Energy released by fires across the continent, in a manner akin to that shown in Fig. 18.13 for a single fire. This FRE total is then converted into an estimate of fuel consumption using Eq. (18.10) and the 'combustion factor' (C, kg MJ^{-1}) derived in Fig. 18.12. The 'Integrated FRE-BA' approach combines the SEVIRI-derived FRE estimates with burned area maps from the MODIS sensor, in order to attempt to adjust the FRE-only estimate for the non-detection of some fire events, due for example to their being low-FRP events or burning under cloud cover (Roberts et al. 2011). The 'GFEDv3' approach is based on the MODIS burned area maps alone (no FRE data) combined via a version of Eq. (18.9) with estimates of fuel load (β, g m^{-2}), derived from the CASA ecosystem production model, and combustion completeness (γ, unitless) derived from e.g. soil moisture estimates (van der Werf et al. 2010). Integrating the burned area maps with the FRE observations results in a fuel consumption estimate closer to that of GFED version 3

Roy (2009), in this case attempting to limit the impact of the lower temporal resolution sampling provided by MODIS rather than the lower spatial resolution sampling provided from geostationary orbit.

18.6.3 Sub-pixel Fire Characteristics

In addition to the estimation of fire radiative power and energy, the primary additional active fire characteristic directly derivable from spaceborne and airborne thermal remote sensing is the 'fire effective' temperature and (sub-pixel) active fire area (Dozier 1981; Robinson 1991; Giglio and Kendall 2001). Note that 'area' in this sense does not refer to the size of the burn scar, but rather the instantaneous area undergoing (flaming and/or smoldering) combustion at the time of thermal image acquisition. Of course, a single temperature and active fire area cannot precisely match the multi-thermal component structure of an actual vegetation fire, so these metrics instead can be viewed as representing the temperature and size of a perfect IR emitter that would provide the same spectral signal as observed from the active fire itself. Nevertheless, despite being an oversimplification of the actual fire situation, such data may be useful in a variety of wildfire measurement and/or modeling scenarios (Zhukov et al. 2006; Dennison et al. 2006; Freitas et al. 2007; Eckmann et al. 2008; Reid et al. 2009).

The primary approach taken to derive the 'fire effective' temperature and (sub-pixel) area is the bi-spectral (or 'dual band') method of Dozier (1981), originally developed to support sub-pixel hotspot detection (Robinson 1991). The technique is based upon measurements of infrared spectral radiance made at two (or sometimes more) well-separated wavelengths, most often with regard to active fires in the MIR and LWIR spectral regions. The same method is also commonly used for analysis of volcanic IR spectral radiance data, though SWIR wavebands are more commonly used in the volcanological case (e.g. Rothery et al. 1988; Francis and Rothery 2000; Ramsey and Harris 2012).

Robinson (1991), Giglio and Kendall (2001), Wooster et al. (2003) and Zhukov et al. (2006) provide great detail on the theory of the bi-spectral method applied to vegetation fire analysis. Assuming blackbody fire behavior, and given the spectral radiance (L_λ) measured at a detected fire pixel in waveband λ, along with a radiance estimate for the non-fire fraction of the fire pixel ($L_{\lambda,bg}$) obtained from surrounding non-fire pixels, the following equation can be formulated for two different wavebands and thus solved to provide an estimate of the fire's effective temperature (T_f) and sub-pixel areal proportion (p_f):

$$L_\lambda = p_f \tau_\lambda B\left(\lambda, T_f\right) + \left(1 - p_f\right) L_{\lambda,bg} + p_f L_\lambda^{\uparrow atm} \tag{18.8}$$

Where $B(\lambda,T)$ is the Planck function (W m^{-2} sr^{-1} μm^{-1}) for waveband λ and temperature T, and τ_λ and $L_\lambda^{\uparrow atm}$ are respectively the atmospheric transmissivity and upwelling atmospheric radiance in that spectral band. The last term will always be small compared to one of the first two terms, and can thus be neglected, enabling the 'fire effective' temperature (T_f) and proportion (P_f) to be retrieved using versions of Eq. (18.8) operating in two different wavebands.

Giglio and Kendall (2001) and Giglio and Justice (2003) provide great detail on the bi-spectral approach, including on limitations related to uncertainties in the ambient background signal at LWIR wavelengths, where the fire signal is typically very much weaker (see Figs. 18.2, 18.3, and 18.4). Additional problems potentially arise from imprecise co-registration between the two spectral channels used, and/or large differences in their point spread function (Langaas 1995). Shephard and Kennelly (2003) modeled the potentially large magnitude of these geometric errors, but Zhukov et al. (2006) suggest they can be largely mitigated against by applying the bi-spectral technique to the average spectral radiances measured at hotspot clusters, rather than at individual fire pixels. Many researchers continue to use the

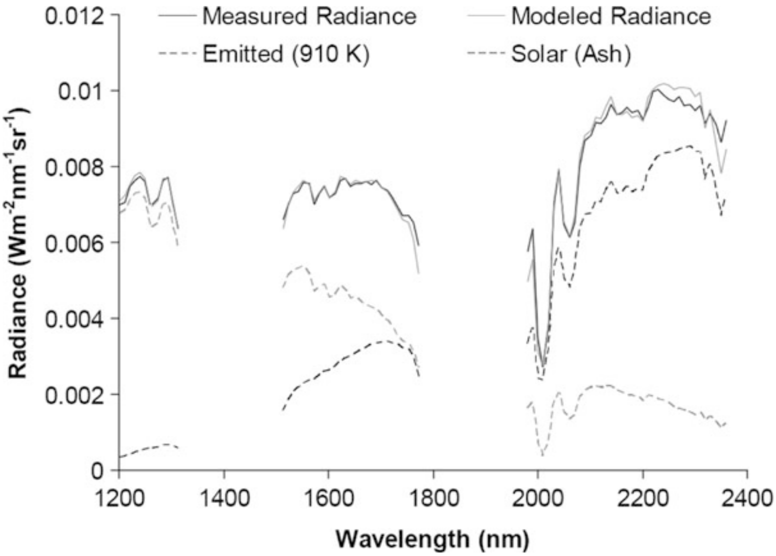

Fig. 18.16 Spectral fits between the measured spectral radiance recorded at an active fire pixel by the airborne AVIRIS instrument, and the modeled best-fit spectrum (calculated as a function of emitted and solar reflected spectral signals). Minimisation of the residuals between the measured and best-fit modeled spectrum allows fire characteristics (e.g. 'fire effective' temperature and sub-pixel size) controlling the emitted radiance component of the measured spectrum to be retrieved (Figure adapted from Dennison et al. 2006)

bi-spectral approach (e.g. Qian and Kong 2012), and the fire effective temperature output from the method may hold some relevance when attempting to discriminate different combustion zones or combustion effects, for example areas of predominantly flaming or smoldering activity or different levels of soil heating (Zhukov et al. 2006; Hanley and Fenner 1998). Similarly, the fire effective area has been used within models of smoke plume injection height (Freitas et al. 2007) and to estimate the fraction of pixels that are releasing smoke into the atmosphere (Reid et al. 2009). Of course, T_f and p_f can also be used together to estimate FRP via the Stefan Boltzman Law (e.g. Wooster et al. 2003).

Alternative approaches to the estimation of subpixel fire effective temperature and area also exist, including those related to the work of Green (1996) and others who used the shape and magnitude of the spectra recorded at active fire pixels by the AVIRIS imaging spectrometer to deduce active fire properties. Dennison et al. (2006) built on this approach to 'unmix' AVIRIS active fire pixel signals into a combination of subpixel (endmember) features (Fig. 18.16). This 'multiple endmember spectral mixture analysis' (MESMA) method was later adapted for use with imagery from alternative IR imaging sensors, such as MODIS (Eckmann et al. 2008) and the HYPER–SIM.GA (Galileo Avionica Multisensor Hyperspectral System) imager whose active fire spectral were shown in Fig. 18.1 (Amici et al. 2011).

18.7 Carbon, Trace Gas and Aerosol Emissions Calculations

Once information on the location and thermal characteristics of actively burning fires have been obtained from the types of remote sensing approaches detailed in the preceding sections, a variety of downstream information can be calculated, for example the rate of spread, (radiative) fireline intensity, and head fire or backfire classification, based on various spatio-temporal analyses of the active fire detection and FRP records (e.g. Smith and Wooster 2005). But perhaps the most significant application is related to estimation of pyrogenic carbon, trace gas and aerosol emissions (e.g. Riggan et al. 2004; Roberts et al. 2009; Kaiser et al. 2012).

Conventional calculations aimed at estimating the mass (M_x) of a particular chemical species x released in a smoke plume are generally based on a multiplication of the amount of biomass burned (kg) by an emissions factor (EF_x, g kg^{-1}). Tables of EF_x for different environments and for dozens of different chemical species present in biomass burning plumes are available in papers such as Andreae and Merlet (2001) and Akagi et al. (2011), so the primary task is to reliably estimate M_x. The approach of Seiler and Crutzen (1980), which in fact was very similar to the original calculations made by von Danckelman (1884), was to determine the amount of biomass burned via the multiplication of burned area (A, m^2), fuel load per unit area (β, g m^{-2}), and the fraction of the available fuel that burns (γ, on a 0–1.0 scale):

$$M_x = A \times \beta \times \gamma \times EF_x \tag{18.9}$$

As satellite-derived burned area estimates have been refined through use of increased spatial resolution datasets and improved burned area detection algorithms (see Sect. 18.5), attention has turned toward uncertainties in the pre-burn fuel load and combustion completeness, which possibly exceed 100 % in some circumstances (Reid et al. 2009; Knorr et al. 2012). To help tackle this limitation, independent estimates of total fuel consumption are often welcomed, at the very least for comparison to those derived via the approach. Results such as those shown in Fig. 18.12 indicate that fire radiative energy (FRE) should be linearly related to the mass of fuel consumed in a fire (Wooster et al. 2005; Freeborn et al. 2007), and use of an FRE measure and a simple 'combustion factor' C (kg MJ^{-1}) therefore allows Eq. (18.9) to be replaced by:

$$M_x = FRE \times C \times EF_x \tag{18.10}$$

The FRP time series for a single African fire was shown in Fig. 18.13, and in this case the FRE and equivalent biomass consumption was estimated as 12×10^6 MJ and ~4,400 ton respectively. Roberts et al. (2009) include comparisons between a set of such FRE-derived fuel consumption estimates and those derived from burned area measures and pre-fire fuel loads, indicating a reasonably linear relationship

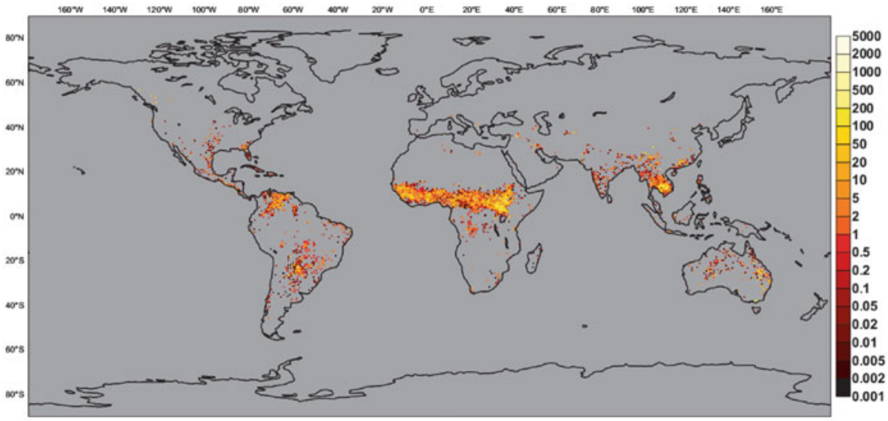

Fig. 18.17 Example global active fire FRP data record for 19 January 2013, produced by the prototype GMES Atmospheric Service currently being developed by the Monitoring Atmospheric Composition and Climate (MACC II) project (URL8). The widespread nature of biomass burning activity is easily seen in this global view. The data represent the daily average of the Fire Radiative Power (*FRP*) observations made from all active fires detected on this day in 125 km grid cells and expressed in units of FRP divided by grid-cell area [mW/m^2] (max. value 0.49 W/m^2). Since the rate of release of thermal radiation by a fire is believed to be related to the rate at which fuel is being consumed and thus smoke produced (see e.g. Fig. 18.12), these data are used for the global estimation of open vegetation fire trace gas and particulate emissions, which are then passed onto the other MACC services for incorporation as model source terms. Publically available data are at present mostly derived from FRP observations made by the MODIS instruments, and future increases in temporal resolution beyond daily averages are planned via use of geostationary FRP products. Products and examples of severe atmospheric perturbation by fire emissions can be found at URL9 and the reader is referred to Kaiser et al. (2012) for further details

between the two approaches. The fire radiative power approach to estimating emissions of carbon, trace gases and aerosols has now reached semi-operational status in the prototype Global Monitoring of Environment and Security (GMES) Atmospheric Service (URL8), currently planned to become operational around 2014. Figure 18.17 shows a map of global 'fire radiative power areal density' (mW m^{-2}) produced by the Global Fire Assimilation System (GFAS) of the GMES Atmospheric Service. The GFAS system uses spaceborne FRP observations to map the daily global release of 40 gas-phase and aerosol trace species present within biomass burning smoke, based on an adaptation of Eq. (18.10) (Kaiser et al. 2012). The system presently assimilates only MODIS FRP observations, and spatially varying adjustments to the 'combustion factor' C have been calculated for different land cover types via a comparison between the FRP-derived metrics calculated by GFAS and version 3 of the GFED database. The resulting emissions fields are fed into a variety of regional and global atmospheric chemistry transport models, supporting near-real time decision making and policy development, including for air quality applications (see URL9 for examples).

18.8 Summary, Conclusions and Some Recommendations

This chapter has demonstrated the basic principles and developments in the thermal remote sensing of active fires, and has reviewed some of the ways in which the resultant datasets have contributed to both (i) a research agenda, aimed for example at better quantification of the amount and variability of worldwide biomass burning, studying its behavior and effects on both the land and atmosphere, and (ii) an operational agenda related to both fire management and fire suppression, and to the monitoring (and sometimes forecasting) of the effects of biomass burning events on the land surface, atmospheric composition, air quality and climate. The prototype GMES Atmospheric Service (URL8) is just one example of how active fire satellite thermal remote sensing now directly supports real-time operational monitoring and management of biomass burning impacts in this way, another being the FLAMBE (Fire Locating and Modeling of Burning Emissions) system described in Reid et al. (2009). The active fire information available in real-time from systems such as FIRMS (URL1) and the EUMETSAT Land Satellite Applications Facility (URL2) also support other, sometimes unexpected, applications. For example, whilst the use of active fire detections in the planning of vegetation management strategies to aid future fire severity reductions might perhaps be foreseen, their use by the South African power company Eskom in avoiding damage from fire-induced “flashover” events in power distribution systems seems far from obvious (Davies et al. 2009).

The 2000s have seen a strong degree of growth in the use of thermal remote sensing to study vegetation fires and biomass burning events. According to an analysis using Google Scholar, prior to 1998 there were fewer than 100 journal articles including the words “active fire” published annually, but that number has grown in a strong linear trend ($r^2 = 0.97$, $n = 14$) to ~600 $year^{-1}$ currently. This growth has most likely been driven both by the availability of new datasets, including most importantly from the highly successful NASA Earth Observing System (EOS) and the accompanying publically available data records (Kaufman et al. 1998b), and by the increasing realization that even relatively spatially limited fire events such as the 1997–1998 fires on Borneo and Sumatra can significantly affect the environment at regional (e.g. Mott et al. 2005) and global scales (Page et al. 2002; Simmonds et al. 2005).

Further developments in sensor technologies and observing systems will be one of the key drivers of future active fire remote sensing. Spaceborne systems such as the proposed Hyperspectral Infrared Imager (HyspIRI; URL10) offer more thermal bands with improved performance with regard to active fire observations than are available currently from systems such as Landsat ETM+ (Enhanced Thematic Mapper Plus) and ASTER. The next generation of imagers onboard the operational GOES and Meteosat satellites will also provide significant benefits for active fire observation. Planning for each of these includes one or more ‘low gain’ thermal bands, somewhat akin to the current MODIS Band 21 ‘fire channel’ (Kaufman et al. 1998b), which should allow unsaturated thermal observations of even very large and/or intensely burning fires. The forthcoming Sentinel-3 SLSTR (Sea and Land Surface Temperature Radiometer) instrument, which follows on from the long-standing (A) ATSR series, also offers a similar capability (Wooster et al. 2012).

Being a rapidly changing, somewhat transient phenomena, validation of active fire observations is in some ways more difficult than for longer-lived occurrences such as burn scars. Validation of the MODIS active fire detection products was greatly aided by the presence of the higher spatial resolution ASTER thermal sensor onboard the same Terra platform, albeit with ASTER's spatial coverage limited to coverage of the central region of the MODIS swath (Morisette et al. 2005; Schroeder et al. 2008a, b). Validation remains an important research focus, not only in terms of active fire detections, but also in terms of the outputs from fire characterization algorithms. The efficacy of metrics such as 'fire effective' temperature and area' deduced via the Dozier (1981) or similar sub-pixel analysis techniques (Sect. 18.6) has received relatively little scrutiny compared to active fire detection accuracy, in part because of their difficulty of validation and because they are in any case only approximations to the true heterogeneous reality existing within fires. This situation is rather similar to that of satellite volcanology, where strategies using very high spatial resolution handled (FLIR) observations have been employed to at least validate some of the assumptions made when using such sub-pixel analysis methods (e.g. Wright and Flynn 2003). Coordinated under flights of satellites with manned aircraft or UAVs carrying more sophisticated thermal sensors is another avenue for cross-comparison, similar to that conducted during SAFARI-2000 shortly after MODIS launch (Swap et al. 2002). This should be repeated for different environments now that data processing chains are more mature.

In addition to validating the algorithms themselves, another key requirement is gaining confidence in the parameters used to quantify fuel consumption and biomass burning emissions. For example, increasing use of fire radiative power and energy approaches requires that the combustion factor (C, kg MJ^{-1}; Sect. 18.6) be verified beyond the limited range of fuels and small fires investigated so far (e.g. Wooster et al. 2005; Freeborn et al. 2008), and the impacts of attenuation by smoke, the ambient atmosphere and vegetation canopies (particularly for surface fires) should gain increased consideration (Kaiser et al. 2012). The optimization of emissions factors (EF_x; see Sect. 18.7) used in deriving chemical emissions estimates from measures of fuel consumption will also continue, driven by required improvements in plume chemistry and transport modelling (e.g. Van Leeuwen and van der Werf 2011). Estimates of fuel moisture, fuel load, fire severity, FRP, and perhaps metrics resulting from other existing or as yet undeveloped fire characterization methods may all have a part to play in such optimization.

The outputs from emissions monitoring and modelling systems (e.g. the GMES Atmospheric Service and FLAMBE) should be continuously evaluated against more direct atmospheric constituent observations (e.g. from satellite, aircraft, tall tower or lidar-based systems; Kaiser et al. 2012), and research into methods to adjust for the limited temporal sampling provided by polar orbiting systems, and/or the non-detection of smaller/lower FRP fires, needs to be continued (Vermote et al. 2009; Ellicott et al. 2009; Boschetti and Roy 2009; Freeborn et al. 2009, 2010; Roberts et al. 2011). Here, the development of 'fire-targeted' satellite remote sensing missions, such as TET-1 (Technology Experiment Carrier 1) and BIROS (Berlin InfraRed Optical System) (Roemer and Halle 2010) can very likely contribute, telling us the frequency distribution of different fire types (Zhukov et al. 2006).

Current BIRD HSRS data suggest that fires having FRP < 10 MW are by far the most common, but are often missed by MODIS class sensors. These data also suggest that such fires are responsible for only a few percent of globally observed total FRP (Zhukov et al. 2006), so the impact of these omissions could be limited. However, the same records indicate that fires with FRP below 100 MW are also responsible for only ~7 % of the global FRP record, which seems incompatible with indications of a roughly two-fold difference between the amount of FRP detected by MODIS and by geostationary systems during long duration, simultaneous sampling periods (Roberts and Wooster 1998; Freeborn et al. 2009). The fact that the BIRD mission preferentially targeted large fire events is one possible cause of these discrepancies, and missions like TET-1, BIROS and future higher resolution thermal imagers such as HyspIRI should ideally be used to evaluate the true situation.

Beyond the above suggestions, further objectives come from the 'Global Observation of Forest Cover and Land Cover Dynamics' (GOFC-GOLD) initiative (URL11), which in addition to a focus on data availability, quality and validity is stimulating the development of a 'geostationary active fire network' to provide almost continuous coverage of fire at lower latitudes, albeit currently with the low-spatial resolution bias associated with geostationary observations. GOFC-GOLD is also highlighting the need for continued production of long-term datasets for better climate-relevant records, against which potential changes in fire regimes may be tested (e.g. Krawchuk et al. 2009). The MODIS data record demonstrates a very strong start in this area, as does the ATSR World Fire Atlas that contains a global record of active fire detections back to 1995 made using a simple nighttime fixed thresholding approach (Mota et al. 2006). It is possible that exploitation of the long-term AVHRR data record, at least for some areas and 'extreme fire' periods warrants further attention (e.g. Cahoon et al. 1994; Stroppiana et al. 2000), particularly after adjusting for differing levels of cloud cover and satellite overpass times (e.g. Wooster et al. 2012).

At the time of writing, the active fire product from the new Visible/Infrared Imager Radiometer Suite (VIIRS) sensor, building on the MODIS experience and flying onboard the NPOESS (National Polar-orbiting Operational Environmental Satellite System) Preparatory Project Suomi satellite, is undergoing testing and calibration (URL7). The VIIRS sensor, along with the ESA Sentinel-3 SLSTR and future 'fire-capable' geostationary imagers, are planned to provide operational active fire datasets for the next two decades. This should stimulate the development of new algorithms and analysis methods, which will likely influence the next generation of spaceborne and airborne sensors for Earth system monitoring, along with their exploitation in continued active fire research and fire management operations.

Acknowledgements The authors would like to thank everyone who provided figures for use in the chapter, the funding agencies who supported the work covered here, and the reviewers for their supportive and useful comments. Martin Wooster was partly supported by the NERC National Centre for Earth Observation (UK) and the European Union's Seventh Framework Programme (FP7/2007–2013) under Grant Agreement no. 283576 (MACC-II project). Alistair Smith is partly supported by NASA under award number NNX11AO24G and the National Science Foundation under award number EPS-0814387.

References

Àgueda A, Pastor E, Perez Y, Planas E (2010) Experimental study of the emissivity of flames resulting from the combustion of forest fuels. Int J Therm Sci 49(3):543–554

Akagi SK, Yokelson RJ, Wiedinmyer C, Alvarado MJ, Reid JS, Karl T, Crounse JD, Wennberg PO (2011) Emission factors for open and domestic biomass burning for use in atmospheric models. Atmos Chem Phys 11(9):4039–4072

Alexander ME (1982) Calculating and interpreting forest fire intensities. Can J Bot 60(4):349–357

Ambrosia VG, Brass JA, Allen JB, Hildum EA, Higgins RG (1994) AIRDAS, development of a unique four channelscanner for natural disaster assessment. In: Proceedings of the first international airborne remote sensing conference, Strasbourg, 11–15 Sept 1994, pp 129–141

Ambrosia VG, Wegener SS, Sullivan DV, Buechel SW, Dunagan SE, Brass JA, Stoneburner J, Schoenung SM (2003) Demonstrating UAV-acquired real-time thermal data over fires. Photogramm Eng Remote Sens 69(4):391–402

Amici S, Wooster MJ, Piscini A (2011) Multi-resolution spectral analysis of wildfire potassium emission signatures using laboratory, airborne and spaceborne remote sensing. Remote Sens Environ 115(8):1811–1823

Andreae MO, Merlet P (2001) Emission of trace gases and aerosols from biomass burning. Glob Biogeochem Cycle 15(4):955–966. doi:10.1029/2000GB001382

Barbosa PM, Grégoire J-M, Pereira JMC (1999) An algorithm for extracting burned areas from time series of AVHRR GAC data applied at a continental scale. Remote Sens Environ 69(3):253–263. doi:10.1016/S0034-4257(99)00026-7

Baum BA, Trepte Q (1999) A grouped threshold approach for scene identification in AVHRR imagery. J Atmos Ocean Technol 16(6):793–800

Becker F, Li Z (1990) Temperature independent spectral indices in thermal infrared bands. Remote Sens Environ 32(1):17–33

Bond WJ, Keeley JE (2005) Fire as a global ‘herbivore’: the ecology and evolution of flammable ecosystems. Trends Ecol Evol 20(7):387–394. doi:10.1016/j.tree.2005.04.025

Bond WJ, van Wilgen BW (1996) Fire and plants. Chapman & Hall, New York

Bond WJ, Woodward FI, Midgley GF (2005) The global distribution of ecosystems in a world without fire. New Phytol 165(2):525–538. doi:10.1111/j.1469-8137.2004.01252.x

Boschetti L, Roy DP (2009) Strategies for the fusion of satellite fire radiative power with burned area data for fire radiative energy derivation. J Geophys Res 114:D20302. doi:10.1029/2008JD011645

Boulet P, Parent G, Acem Z, Collin A, Séro-Guillaume O (2011) On the emission of radiation by flames and corresponding absorption by vegetation in forest fires. Fire Saf J 46(1–2):21–26

Bowman DMJS, Balch JK, Artaxo P, Bond WJ, Carlson JM, Cochrane MA, D’Antonio CM, DeFries RS, Doyle JC, Harrison SP, Johnston FH, Keeley JE, Krawchuk MA, Kull CA, Marston JB, Moritz MA, Prentice IC, Roos CI, Scott AC, Swetnam TW, van der Werf GR, Pyne SJ (2009) Fire in the earth system. Science 324(5926):481–484. doi:10.1126/science.1163886

Boyd DS, Petitcolin F (2004) Remote sensing of the terrestrial environment using middle infrared radiation (3.0–5.0 μm). Int J Remote Sens 25(17):3343–3368. doi:10.1080/01431160310001654356

Brönnimann S, Volken E, Lehmann K, Wooster MJ (2009) Biomass burning aerosols and climate – a 19th century perspective. Meteorol Z 18:349–353

Budd GM, Brotherhood JR, Hendrie AL, Jeffery SE, Beasley FA, Costin BP, Zhien W, Baker MM, Cheney NP, Dawson MP (1997) Project Aquarius 4. Experimental bushfires, suppression procedures, and measurements. Int J Wildland Fire 7(2):99–104. doi:10.1071/WF9970099

Byram M (1959) Combustion of forest fuels. In: Davis KP (ed) Forest fire: control and use. McGraw-Hill, New York, pp 61–89

Cahoon DR, Stocks BJ, Levine JS, Cofer WR, Pierson JM (1994) Satellite analysis of the severe 1987 forest fires in northern China and southeastern Siberia. J Geophys Res 99(D9):18627–18638

Cheney P, Sullivan A (2008) Grassfires: fuel, weather and fire behaviour. CSIRO Publishing, Melbourne, 150 p

Cochrane MA (2003) Fire science for rainforests. Nature 421:913–919. doi:10.1038/nature01437

Coheur PF, Clarisse L, Turquety S, Hurtmans D, Clerbaux C (2009) IASI measurements of reactive trace species in biomass burning plumes. Atmos Chem Phys 9:5655–5667
Crutzen PJ, Andreae MO (1990) Biomass burning in the tropics: impact on atmospheric chemistry and biogeochemical cycles. Science 250:1669–1678
Davies DK, Ilavajhala S, Wong MM, Justice CO (2009) Fire information for resource management system: archiving and distributing MODIS active fire data. IEEE Trans Geosci Remote Sens 47(1):72–79
De Bano LF, Neary DG, Ffolliott PF (1998) Fire's effects on ecosystems. Wiley, Chichester
Dennison PE, Charoensiri K, Roberts DA, Peterson SH, Green RO (2006) Wildfire temperature and land cover modeling using hyperspectral data. Remote Sens Environ 100:212–222. doi:10.1016/j.rse.2005.10.007
Di Bella CM, Jobbágy EG, Paruelo JM, Pinnock S (2006) Continental fire density patterns in South America. Glob Ecol Biogeogr 15:192–199. doi:10.1111/j.1466-822x.2006.00225.x
Dietenberger M (2002) Update for combustion properties of wood components. Fire Mater 26(6):255–267
Dipert D, Warren JR (1988) Mapping fires with the FIRE MOUSE TRAP. Fire Manag Note US Dep Agric 49(2):28–30
Dozier J (1981) A method for satellite identification of surface temperature fields of subpixel resolution. Remote Sens Environ 11:221–229
Eckmann TC, Roberts DA, Still CJ (2008) Using multiple endmember spectral mixture analysis to retrieve subpixel fire properties from MODIS. Remote Sens Environ 112(10):3773–3783
Ellicott E, Vermote E, Giglio L, Roberts G (2009) Estimating biomass consumed from fire using MODIS FRE. Geophys Res Lett 36(13):1–5
Elvidge CD, Kroehl HW, Kihn EA, Baugh KE, Davis ER, Hao WM (1996) Algorithm for retrieval of fire pixels from DMSP operational linescan system data. In: Levine JS (ed) Biomass burning and global change, vol 1, Remote sensing, modeling and inventory development, and biomass burning in Africa. MIT Press, Cambridge, MA, pp 73–85
Eva H, Lambin EF (1998) Burnt area mapping in Central Africa using ATSR data. Int J Remote Sens 19(18):3473–3497. doi:10.1080/014311698213768
Flannigan MD, Vonder Haar TH (1986) Forest fire monitoring using NOAA satellite AVHRR. Can J For Res 16:975–982
Flasse SP, Ceccato P (1996) A contextual algorithm for advanced very high resolution radiometer (AVHRR fire detection). Int J Remote Sens 17(2):419–424. doi:10.1080/01431169608949018
Francis P, Rothery DA (2000) Remote sensing of active volcanoes. Annu Rev Earth Planet Sci 28:81–106
Fraser RH, Li Z, Cihlar J (2000) Hotspot and NDVI differencing synergy (HANDS): a new technique for burned area mapping over boreal forest. Remote Sens Environ 74:362–376. doi:10.1016/S0034-4257(00)00078-X
Freeborn P, Wooster MJ, Hao WM, Ryan CA, Nordgren BL, Baker SP, Ichoku C (2008) Relationships between energy release, fuel mass loss, and trace gas and aerosol emissions during laboratory biomass fires. J Geophys Res 113:D01301. doi:10.1029/2007JD008679
Freeborn PH, Wooster MJ, Roberts G, Malamud BD, Xu W (2009) Development of a virtual active fire product for Africa through a synthesis of geostationary and polar orbiting satellite data. Remote Sens Environ 113(8):1700–1711
Freeborn PH, Wooster MJ, Roberts G (2010) Addressing the spatiotemporal sampling design of MODIS to provide estimates of the fire radiative energy emitted from Africa. Remote Sens Environ 115(2):45–489
Freitas SR, Longo KM, Chatfield R, Latham D, Silva Dias MAF, Andreae MO, Prins E, Santos JC, Gielow R, Carvalho JA Jr (2007) Including the sub-grid scale plume rise of vegetation fires in low resolution atmospheric transport models. Atmos Chem Phys 7:3385–3398
Giglio L (2007) Characterization of the tropical diurnal fire cycle using VIRS and MODIS observations. Remote Sens Environ 108(4):407–421. doi:10.1016/j.rse.2006.11.018
Giglio L (2010) MODIS collection 5 active fire product user's guide, version 2.4. Department of Geography, University of Maryland

Giglio L, Justice CO (2003) Effect of wavelength selection on characterization of fire size and temperature. Int J Remote Sens 24(17):3515–3520

Giglio L, Kendall JD (2001) Application of the Dozier retrieval to wildfire characterization: a sensitivity analysis. Remote Sens Environ 77:34–49

Giglio L, Kendall JD, Justice CO (1999) Evaluation of global fire detection algorithms using simulated AVHRR infrared data. Int J Remote Sens 20(10):1947–1985. doi:10.1080/014311699212290

Giglio L, Kendall JD, Tucker CJ (2000) Remote sensing of fires with the TRMM VIRS. Int J Remote Sens 21(1):203–207

Giglio L, Descloitres J, Justice CO, Kaufman YJ (2003) An enhanced contextual fire detection algorithm for MODIS. Remote Sens Environ 87:273–282. doi:10.1016/S0034-4257(03)00184-6

Giglio L, van der Werf GR, Randerson JT, Collatz GJ, Kasibhatla P (2006) Global estimation of burned area using MODIS active fire observations. Atmos Chem Phys 6:957–974

Giglio L, Randerson JT, van der Werf GR, Kasibhatla PS, Collatz GJ, Morton DC, DeFries RS (2010) Assessing variability and long-term trends in burned area by merging multiple satellite fire products. Biogeosciences 7:1171–1186

Giglio L, Loboda T, Roy DP, Quayle B, Justice CO (2009) An active-fire based burned area mapping algorithm for the MODIS sensor. Remote Sens Environ 113(2):408–420

Giriraj A, Babar S, Jentsch A, Sudhakar S, Murthy M (2010) Tracking fires in India using Advanced Along Track Scanning Radiometer (AATSR) data. Remote Sens 2:591–610

Green RO (1996) Estimation of biomass fire temperature and areal extent from calibrated AVIRIS spectra. Summ Sixth Annu JPL Airborne Earth Sci Workshop JPL Publ 96(4):105–113

Hanley ME, Fenner M (1998) Pre-germination temperature and the survivorship and onward growth of Mediterranean fire-following plant species. Acta Oecol 19:181–187

Hirsch SN, Madden FH (1969) Airborne infrared line scanners for forest fire surveillance. In: 14th SPIE Annual technical symposium proceedings, vol 2, pp 51–57

Holden Z, Smith AMS, Morgan P, Rollins MG, Gessler PE (2005) Evaluation of novel thermally enhanced spectral indices for mapping fire perimeters and comparisons with fire atlas data. Int J Remote Sens 26(21):4801–4808

Hook SJ, Myers JJ, Thome KJ, Fitzgerald M, Kahle AB (2001) The (MASTER) – a new instrument for earth science studies. Remote Sens Environ 76(1):93–102

Ichoku C, Kaufman YJ (2005) A method to derive smoke emission rates from MODIS fire radiative energy measurements. IEEE Trans Geosci Remote Sens 43(11):2636–2649. doi:10.1109/TGRS.2005.857328

Jacobson MC, Hansson H-C, Noone KJ, Charlson RJ (2000) Organic atmospheric aerosols: review and state of the science. Rev Geophys 38(2):267–294

Jenkins BM, Baxter LL, Miles TR Jr, Miles TR (1998) Combustion properties of biomass. Fuel Proc Technol 5491:17–46

Justice CO, Kendall JD, Dowty PR, Scholes RJ (1996) Satellite remote sensing of fires during the SAFARI campaign using NOAA AVHRR data. J Geophys Res 101:23851–23863

Kaiser JW, Heil A, Andreae MO, Benedetti A, Chubarova N, Jones L, Morcrette J-J, Razinger M, Schultz MG, Suttie M, van der Werf GR (2012) Biomass burning emissions estimated with a global fire assimilation system based on observed fire radiative power. Biogeosciences 9:527–554. doi:10.5194/bg-9-527-2012

Kaufman YJ, Remer LA (1994) Detection of forests using MID-IR reflectance – an application for aerosol studies. IEEE Trans Geosci Remote Sens 32(3):672–683

Kaufman Y, Justice C, Flynn L, Kendall J, Prins E, Giglio L, Ward D, Menzel W, Setzer A (1998a) Potential global fire monitoring from EOS-MODIS. J Geophys Res 103(D24):32215–32238

Kaufman Y, Kleidmann RG, King MD (1998b) SCAR-B fires in the tropics: properties and remote sensing from EOS-MODIS. J Geophys Res 103(D24):31955–31968

Kaufman YJ, Tanre D, Boucher O (2002) A satellite view of aerosols in the climate system. Nature 419(6903):215–223

Knorr W, Lehsten V, Arneth A (2012) Determinants and predictability of global wildfire emissions. Atmos Chem Phys Discuss 12:4243–4278. doi:10.5194/acpd-12-4243-2012

Krawchuk MA, Moritz MA, Parisien M-A, Van Dorn J, Hayhoe K (2009) Global pyrogeography: the current and future distribution of wildfire. PLoS One 4(4):e5102. doi:10.1371/journal.pone.0005102

Kunii O, Kanagawa S, Yajima I, Hisamatsu Y, Yamamura S, Amagai T, Ismail ITS (2002) The 1997 haze disaster in Indonesia: its air quality and health effects. Arch Environ Health 57(1):16–22

Langaas S (1995) A critical review of sub-resolution fire detection techniques and principles using thermal satellite data. University of Oslo, Oslo

Lavorel S, Flannigan MD, Lambin EF, Scholes MC (2007) Vulnerability of land systems to fire: interactions among humans, climate, the atmosphere, and ecosystems. Mitig Adapt Strat Glob Chang 12(1):33–53. doi:10.1007/s11027-006-9046-5

Lentile LB, Holden ZA, Smith AMS, Falkowski MJ, Hudak AT, Morgan P, Lewis SA, Gessler PE, Benson NC (2006) Remote sensing techniques to assess active fire characteristics and post-fire effects. Int J Wildland Fire 15(3):319–345. doi:10.1071/WF05097

Li Z, Kaufman YJ, Ichoku C, Fraser R, Trishchenko A, Giglio L, Jin J (2002) A review of AVHRR-based active fire detection algorithms: principles, limitations, and recommendations. In: Ahern FJ, Goldammer JG, Justice CO (eds) Global and regional vegetation fire monitoring from space: planning and coordinated international effort. SPB Academic Pub, The Hague, pp 199–225

Libonati R, Pereira JMC, Setzer AW, de Faria Peres L (2009) Retrieval of middle-infrared reflectance using remote sensing data: the tropical point of view. In: Simpósio Brasileiro de Sensoriamento Remoto, 14 (SBSR) 2009, pp 5917–5924

Lynch DL (2004) What do forest fires really cost? J For 102(6):42–49

Mayaux P, Bartholomé E, Fritz S, Belward A (2004) A new land-cover map of Africa for the year 2000. J Biogeogr 31(6):861–877

McMillan WW, McCourt WM, Revercomb HE, Knuteson RO, Christian TG, Doddridge BG, Hobbs PV et al (2003) Tropospheric carbon monoxide measurements from the scanning high-resolution interferometer sounder on 7 September 2000 in southern Africa during SAFARI 2000. J Geophys Res 108(D13):8492. doi:10.1029/2002JD002335

Merino L, Caballero F, Martínez-de Dios JR, Ferruz J, Ollero A (2006) A cooperative perception system for multiple UAVs: application to automatic detection of forest fires. J Field Robot 23(3–4):165–184

Morisette JT, Giglio L, Csiszar I, Justice CO (2005) Validation of the MODIS active fire product over Southern Africa with ASTER data. Int J Remote Sens 26(19):4239–4264

Mota BW, Pereira JMC, Oom D, Vasconcelos MJP, Schultz M (2006) Screening the ESA ATSR-2 World Fire Atlas (1997–2002). Atmos Chem Phys 6:1409–1424. doi:10.5194/acp-6-1409-2006

Mott JA, Mannino DM, Alverson CJ, Kiyu A, Hashim J, Lee T, Falter K, Redd SC (2005) Cardiorespiratory hospitalizations associated with smoke exposure during the 1997 Southeast Asian forest fires. Int J Hyg Environ Health 208(1):75–85

Naeher LP, Brauer M, Lipsett M, Zelikoff JT, Simpson CD, Koenig JQ, Smith KR (2007) Woodsmoke health effects: a review. Inhal Toxicol 19(1):67–106

Nichols JD, Parks GS, Voss JM, Mortensen RA, Logan TL (1989) Designing an infrared system to map and detect wildland fires. In: 1989 Orlando symposium. International Society for Optics and Photonics, pp 7–14

Page SE, Siegert F, Rieley JO, Boehm HDV, Jaya A, Limin S (2002) The amount of carbon released from peat and forest fires in Indonesia during 1997. Nature 420:61–65. doi:10.1038/nature01131

Pastor E, Rigueiro A, Zárate L, Giménez A, Arnaldos J, Planas E (2002) Experimental methodology for characterizing flame emissivity of small scale forest fires using infrared thermography techniques, Forest fire research & wildland fire safety. Millpress, Rotterdam

Pausas JG, Keeley JE (2009) A burning story: the role of fire in the history of life. Bioscience 59(7):593–601. doi:10.1525/bio.2009.59.7.10

Pereira JMC, Chuvieco E, Beudoin A, Desbois N (1997) Remote sensing of burned areas: a review. In: Chuvieco E (ed) A review of remote sensing methods for the study of large wildland fires. Departamento de Geografía, Universidad de Alcalá, Alcalá de Henares, pp 127–184

Petitcolni F, Vermote E (2002) Land surface reflectance, emissivity and temperature from MODIS middle and thermal infrared data. Remote Sens Environ 83(1):112–134

Prins EM, Menzel WP (1992) Geostationary satellite detection of biomass burning in South America. Int J Remote Sens 13:2783–2799. doi:10.1080/01431169208904081

Prins EM, Feltz JM, Menzel WP, Ward DE (1998) An overview of GOES-8 diurnal fire and smoke results for SCAR-B and 1995 fire season in South America. J Geophys Res Atmos (1984–2012) 103(D24):31821–31835

Pyne SJ (1984) Introduction to wildland fire: fire management in the United States. Wiley, New York

Qian YG, Kong SX (2012) A method to retrieve subpixel fire temperature and fire area using MODIS data. Int J Remote Sens 33:5009–5025

Ramsey MS, Harris AJL (2012) How will thermal remote sensing of volcanic surface activity evolve over the next decade. J Volcanol Geoth Res 249:217–233. doi:10.1016/j.jvolgeores.2012.05.011

Reid JS, Hyer EJ, Prins EM, Westphal DL, Zhang J, Wang J, Christopher SA, Curtis CA, Schmidt CC, Eleuterio DP, Richardson KA, Hoffman JP (2009) Global monitoring and forecasting of biomass-burning smoke: description of and lessons from the Fire Locating and Modeling of Burning Emissions (FLAMBE) program. IEEE J Sel Top Appl Earth Obs Remote Sens 2 (3):144–162. doi:10.1109/JSTARS.2009.2027443

Riggan PJ, Tissell RG (2009) Airborne remote sensing of wildland fires. In: Bytnerowicz A, Arbaugh M, Andersen C, Riebau A (eds) Wildland fires and air pollution, vol 8, Developments in environmental science. Elsevier, Amsterdam, pp 139–168

Riggan PJ, Tissell RG, Lockwood RN, Brass JA, Pereira JAR, Miranda HS, Miranda AC, Campos T, Higgins RG (2004) Remote measurement of energy and carbon flux from wildfires in Brazil. Ecol Appl 14(3):855–872

Roberts G, Wooster MJ (2008) Fire detection and fire characterization over Africa using Meteosat SEVIRI. IEEE Trans Geosci Remote Sens 46:1200–1218. doi:10.1109TGRS.2008.915751

Roberts G, Wooster MJ, Lagoudakis E (2009) Annual and diurnal African biomass burning temporal dynamics. Biogeosciences 6:849–866. doi:10.5194/bg-6-849-2009

Roberts G, Wooster MJ, Freeborn P, Xu W (2011) Integration of geostationary FRP and polar-orbiter burned area datasets for an enhanced biomass burning inventory. Remote Sens Environ 115:2047–2061. doi:10.1016/j.rse.2011.04.006

Robinson JM (1991) Fire from space: global fire evaluation using infrared remote sensing. Int J Remote Sens 12(1):3–24. doi:10.1080/01431169108929628

Roemer S, Halle W (2010) TET-1 and BIROS a semi-operational fire recognition constellation, UN/Austria/ESA symposium on small satellite programs for sustainable development: payloads for small satellite programs, Graz, 21–24 Sept 2010

Rothery DA, Francis PW, Wood CA (1988) Volcano monitoring using short wavelength infrared data from satellites. J Geophys Res 93:7993–8008

Schroeder W, Prins E, Giglio L, Csiszar I, Schimdt C, Morisette J, Morton D (2008a) Validation of GOES and MODIS active fire detection products using ASTER and ETM+ data. Remote Sens Environ 112(5):2711–2726. doi:10.1016/j.rse.2008.01.005

Schroeder W, Csiszar I, Morisette J (2008b) Quantifying the impact of cloud obscuration on remote sensing of active fires in the Brazilian Amazon. Remote Sens Environ 112(2):456–470. doi:10.1016/j.rse.2007.05.004

Seiler W, Crutzen PJ (1980) Estimates of gross and net fluxes of carbon between the biosphere and the atmosphere from biomass burning. Clim Chang 2:207–247

Shephard MW, Kennelly EJ (2003) Effect of band-to-band coregistration on fire property retrievals. IEEE Trans Geosci Remote Sens 41(11):2648–2661. doi:10.1109/TGRS.2003.814912

Simmonds PG, Manning AJ, Derwent RG, Ciais P, Ramonet M, Kazan V, Ryall D (2005) A burning question. Can recent growth rate anomalies in the greenhouse gases be attributed to large-scale biomass burning events? Atmos Environ 39(14):2513–2517. doi:10.1016/j.atmosenv.2005.02.018

Smith AMS, Wooster MJ (2005) Remote classification of head and backfire types from MODIS fire radiative power observations. Int J Wildland Fire 14:249–254. doi:10.1071/WF05012

Smith AMS, Drake N, Wooster MJ, Hudak A, Holden ZA, Gibbons CJ (2007) Production of Landsat ETM reference imagery of burned areas within Southern African savannahs: comparison of methods and application to MODIS. Int J Remote Sens 28:2753–2775

Stroppiana D, Pinnock S, Gregoire J-M (2000) The global fire product: daily fire occurrence from April 1992 to December 1993 derived from NOAA AVHRR data. Int J Remote Sens 21 (6–7):1279–1288

Stocks BJ, Van Wilgen BW, Trollope WSW (1997) Fire behaviour and the dynamics of convection columns in African savannas. In: Van Wilgen BW, Andreae MO, Goldammer GJ, Lindesay JA (eds) Fire in southern African Savannas: ecological and atmospheric perspectives. Wits University Press, Johannesburg, pp 47–55

Sullivan AL, Ellis PF, Knight IK (2003) A review of radiant heat flux models used in bushfire applications. Int J Wildland Fire 12(1):101–110. doi:10.1071/WF02052

Swap RJ, Annegarn HJ, Suttles JT, Haywood J, Helmlinger MC, Hely C, Hobbs PV, Holben BN, Ji J, King MD, Landmann T, Maenhaut W, Otter L, Pak B, Piketh SJ, Platnick S, Privette J, Roy D, Thompson AM, Ward D, Yokelson R (2002) The Southern African regional science initiative (SAFARI 2000): overview of the dry season field campaign. S Afr J Sci 98:125–130

Trigg S, Flasse S (2000) Characterizing the spectral-temporal response of burned savannah using in situ spectroradiometry and infrared thermometry. Int J Remote Sens 21(16):3161–3168. doi:10.1080/01431160050145045

Trigg SN, Roy DP (2007) A focus group study of factors that promote and constrain the use of satellite derived fire products by resource managers in southern Africa. J Environ Manage 82:95–110

Trollope WSW (2002) Fire behaviour a key factor in the fire ecology of African grasslands and savannas. In: Viegas DX (ed) Forest fire research and wildland fire safety: proceedings of IV international conference on forest fire research/2002 wildland fire safety summit, Coimbra. Millpress, Rotterdam, pp 1–17

Turner MG, Hargrove WW, Gardner RH, Romme WH (1994) Effects of fire on landscape heterogeneity in Yellowstone National Park, Wyoming. J Veg Sci 5(5):731–742

van der Werf GR, Randerson JT, Collatz GJ, Giglio L, Kasibhatla PS, Arellano AF Jr, Olsen SC, Kasischke ES (2004) Continental-scale partitioning of fire emissions during the 1997 to 2001 El Niño/La Niña period. Science 303(5654):73–76. doi:10.1126/science.1090753

van der Werf GR, Morton DC, DeFries RS, Olivier JGJ, Kasibhatla PS, Jackson RB, Collatz GJ, Randerson JT (2009) CO2 emissions from forest loss. Nat Geosci 2:737–738. doi:10.1038/ngeo671

van der Werf GR, Randerson JT, Giglio L, Collatz GJ, Mu M, Kasibhatla PS, Morton DC, DeFries RS, Jin Y, van Leeuwen TT (2010) Global fire emissions and the contribution of deforestation, savanna, forest, agricultural, and peat fires (1997–2009). Atmos Chem Phys 10:11707–11735. doi:10.5194/acp-10-11707-2010

Van Leeuwen TT, van der Werf GR (2011) Spatial and temporal variability in the ratio of trace gases emitted from biomass burning. Atmos Chem Phys 11:3611–3629

Vermote E, Ellicott E, Dubovik O, Lapyonok T, Chin M, Giglio L, Roberts GJ (2009) An approach to estimate global biomass burning emissions of organic and black carbon from MODIS fire radiative power. J Geophys Res 114:D18205

von Danckelman A (1884) Die Bewölkungsverhältnisse des südwestlichen Afrikas. Meteorol Z 1:301–311

Wallace LL (2004) After the fires: the ecology of change in Yellowstone National Park. Yale University Press, New Haven

Ward D (2001) Combustion chemistry and smoke. In: Johnson EA, Miyanishi K (eds) Forest fires: behavior and ecological effects. Academic Press, San Diego, pp 55–77

Warren JR (1992) Advanced fire sensing and locating systems, remote sensing and natural resource management: proceedings of the fourth forest service remote sensing applications conference, 6–11 Apr, Orlando, FL, pp 212–220

Warren JR, Celarier DN (1991) A salute to infrared systems in fire detection and mapping. Fire Manag Note US Dep Agric 52(3):3–18

Wegener SS, Ambrosia VG, Stoneburner J, Sullivan DV, Brass JA, Buechel SW, Higgins RG, Hildum EA, Schoenung SM (2002) Demonstrating acquisition of real-time thermal data over fires utilizing UAVs. In: Proceedings of AIAA's 1st technical conference and workshop on unmanned aerospace vehicles, systems, technologies, and operations, vol AIAA-2002-3406, Portsmouth, VA, 20–23 May 2002

Wooster MJ, Strub N (2002) Borneo fires: quantitative analysis using global area coverage (GAC) satellite data. Glob Biogeochem Cycle 16(1):9. doi:10.1029/2000GB001357

Wooster MJ, Richards T, Kidwell KB (1995) NOAA 11 AVHRR/2 – thermal channel calibration update. Int J Remote Sens 16(2):359–363. doi:10.1080/01431169508954401

Wooster MJ, Zhukov B, Oertel D (2003) Fire radiative energy for quantitative study of biomass burning: derivation from the BIRD experimental satellite and comparison to MODIS fire products. Remote Sens Environ 86:83–107

Wooster MJ, Roberts G, Perry GLW, Kaufman YJ (2005) Retrieval of biomass combustion rates and totals from fire radiative power observations: FRP derivation and calibration relationships between biomass consumption and fire radiative energy release. J Geophys Res 110:D24311. doi:10.1029/2005JD006318

Wooster MJ, Freeborn PH, Archibald S, Oppenheimer C, Roberts GJ, Smith TEL, Govender N, Burton M, Palumbo I (2011) Field determination of biomass burning emission ratios and factors via open-path FTIR spectroscopy and fire radiative power assessment: headfire, backfire and residual smouldering combustion in African savannahs. Atmos Chem Phys 11:11591–11615

Wooster MJ, Perry GLW, Zoumas A (2012) Fire, drought and El Niño relationships on Borneo (Southeast Asia) in the pre-MODIS era (1980–2000). Biogeosciences 9:317–340. doi:10.5194/bg-9-317-2012

Wright R, Flynn LP (2003) On the retrieval of lava-flow surface temperatures from infrared satellite data. Geology 31(10):893–896

Xu W, Wooster MJ, Roberts G, Freeborn PH (2011) New GOES imager algorithms for cloud and active fire detection and fire radiative power assessment across North, South and Central America. Remote Sens Environ 114:1876–1895

Zhukov B, Lorenz E, Oertel D, Wooster MJ, Roberts G (2006) Spaceborne detection and characterization of fires during the bi-spectral infrared detection (BIRD) experimental small satellite mission (2001–2004). Remote Sens Environ 100(1):29–51. doi:10.1016/j.rse.2005.09.019

URL1: http://earthdata.nasa.gov/firms

URL2: http://landsaf.meteo.pt/

URL3: http://lance.nasa.gov

URL4: http://cimss.ssec.wisc.edu/goes

URL5: http://wildfire.geog.kcl.ac.uk/wordpress

URL6: http://www.itres.com

URL7: http://viirsfire.geog.umd.edu

URL8: http://www.gmes-atmosphere.eu/

URL9: http://www.gmes-atmosphere.eu/fire

URL10: http://hyspiri.jpl.nasa.gov/

URL11: http://gofc-fire.umd.edu/objectives/index.php